DOI: 10.1002/cbic.200((will be filled in by the editorial staff))

NMR study of human liver FABP and glycocholate

Ligand binding promiscuity of human liver fatty acid binding protein: structural and dynamic insights from an interaction study with glycocholate and oleate

Filippo Favretto,[a] Michael Assfalg,[a] Mariana Gallo,[b] Daniel Oscar Cicero,[c] Mariapina D'Onofrio,*[a] and Henriette Molinari*[d]

Dedicated to Ivano, the greatest and beloved friend and scientist

Human liver fatty acid binding protein (hL-FABP) has been reported to act as an intracellular shuttle of lipid molecules, playing a central role in systemic metabolic homeostasis. The involvement of hL-FABP in the transport of bile salts has been postulated but scarcely investigated. Here we describe a thorough NMR investigation of glycocholate (GCA) binding to hL-FABP. The protein proved able to bind a single molecule of GCA in contrast with the 1:2 stoichiometry observed with fatty acids. GCA was found to occupy the large internal cavity of hL-FABP without requiring major conformational rearrangements of the protein backbone but leading to an increased stability, similar to that estimated for the hL-FABP:oleate complex. Fast time scale dynamics appeared not significantly perturbed in the presence of ligands. Slow motions, at variance with other proteins of the family, were retained or enhanced upon binding and consistent with a requirement of structural plasticity for promiscuous recognition.

Introduction

Intracellular lipid binding proteins (iLBPs) are essential components of a finely tuned transportation machinery that dictates the fate of lipid molecules in the cells.[1] Evidence is accumulating that iLBPs are playing central roles in cellular lipid transport and metabolism, also being capable of modulating lipid bioactivity.[2] The study of the mechanisms by which lipid carriers bind to their ligands is essential to understand the regulatory role played by these proteins in lipid signaling and systemic metabolic homeostasis, leading to a formulation of their potential therapeutic significance.[3] iLBPs are low molecular weight polypeptides showing significant diversity of primary sequences and exhibiting a distinctive pattern of tissue distribution.[4] They have been categorized into four classes based on sequence homology and ligand binding properties:[5] I) retinoid binding proteins (RBP), II) liver-type fatty acid binding protein (L-FABP) and liver/intestinal bile acid binding proteins (L-BABP, I-BABP), III) intestinal fatty acid binding protein (I-FABP), IV) adipocyte-, brain-, epidermal-, heart-, myelin-type fatty acid binding proteins. It is noteworthy that the tertiary structures are highly conserved among all members of the family,[6,7] consisting in ten antiparallel β-strands that form a clam-shell-like structure, capped by a pair of α-helices. The interior of the proteins contains a cavity serving as a binding pocket for hydrophobic ligands that are specific for different iLBPs.

FABPs have specialized ability to reversibly bind long chain fatty acids (LCFA) with high affinity, generally with a 1:1 stoichiometry.[8] L-FABP is prominent among all FABPs due to several unique features, including its capability to simultaneously bind two molecules of LCFA, as clearly shown by the first three-dimensional structure of rat(r) L-FABP with oleate (OLA).[9] A structural characterization of the human orthologue has curiously not been undertaken until very recently, when several crystal- and solution-state structures of hL-FABP appeared, confirming the general iLBP fold and binding stoichiometry, but also pointing out some controversial results.[10–12] L-FABP is further able to accommodate a variety of bulkier hydrophobic/amphipathic ligands including fatty acyl-CoA thioesters, lysophosphatidic acid, bile salts, heme, eicosanoids, and bilirubin.[13–16] The binding promiscuity of L-FABP is made possible by the largest binding

---

[a] F. Favretto, Dr. M. Assfalg, Dr. M. D'Onofrio
NMR laboratory, Department of Biotechnology
University of Verona
Strada le Grazie 15, 37134 Verona (Italy)
Fax: (+39)0458027929
E-mail: mariapina.donofrio@univr.it

[b] Dr. M. Gallo
Fundación Instituto Leloir, IIBBA-CONICET
Ciudad Autónoma de Buenos Aires, C1405BWE, Argentina

[c] Prof. D.O. Cicero
Department of Chemical Science and Technology
University of Rome ''Tor Vergata''
Rome 00133, Italy

[d] Prof. H. Molinari
Laboratorio NMR, ISMAC-CNR
Via Bassini 15, 20133 Milano (Italy)
Fax: (+39)0223699620
E-mail: henriette.molinari@univr.it

*Supporting information for this article is available on the WWW under http://www.chembiochem.org or from the author.((**Please delete if not appropriate**))* pocket among all FABPs,[17] and has attracted interest for the potential role of L-FABP in the transportation of lipophilic drugs across the liver,[18] as well as for the development of protein-targeted lipid-based intracellular contrast agents for MRI.[19] Due to the extraordinary elevated concentration of L-FABP in the cytosol, accounting for as much as 7-11% of cytosolic protein in normal human liver,[20] it has been estimated that L-FABP may not be saturated by LCFA, thus being available for binding to diverse hydrophobic molecules.[18]

Despite its recognized binding promiscuity, the main body of studies on L-FABP has been focused on its interaction with LCFA, probably the most frequent physiological ligands. However, a central role of L-FABP in the transport of bile salts has also been postulated. It has been shown that ablation of the gene codifying for L-FABP in mice altered the metabolism of cholesterol and bile salts.[21] Furthermore, photoaffinity labeling experiments performed on hepatocyte snips, hepatocyte cytosol, and intact liver tissues demonstrated that rat L-FABP is the essential binding protein ensuring the intracellular transport of sulphated and taurine-conjugated bile salts.[22] In support of this hypothesis is also the realization that L-BABP, a specific bile salt carrier also belonging to subfamily II of iLBPs, is absent in mammalians.[23] The binding of cholesterol, bile salts and their derivatives to rL-FABP has been previously investigated based on fluorescent ligand-displacement assays.[24] Under the used assay conditions cholic (CA) and chenodeoxycholic acids (CDA) were shown to be only mildly effective in displacing the probe from L-FABP, consistent with an estimated dissociation constant K_d > 10 μM.

Direct binding experiments of bile acids to hL-FABP are limited to our previous finding that glycochenodeoxycholate (GCDA), one of the predominating bile salts in the human pool together with glycocholate (GCA), is able to interact with the protein.[23] In this work we aimed at providing a first description of molecular details of the interaction between hL-FABP and putative ligands other than LCFA. We describe a thorough NMR spectroscopy study of GCA binding to hL-FABP, focusing on structural and dynamic aspects of the protein in its bound state. In order to investigate the distinctive features of binding promiscuity, we further present a comparative analysis with hL-FABP alone and in complex with OLA, based on experiments performed in the same conditions and extending previous works. We discuss the results in the frame of current knowledge about protein functional dynamics within the iLBPs family. Our findings also contribute to an understanding of the role of L-FABP in bile salt trafficking.

Results

Ligand-observed titration of hL-FABP with GCA

Amide NMR signals of ^{15}N-enriched glyco-conjugated bile salts have been frequently used as powerful probes of binding to their carrier proteins.[25–30] ^{1}H,^{15}N-heteronuclear single quantum coherence (HSQC) spectra were acquired on hL-FABP added with increasing amounts of [^{15}N]GCA. A low-intensity H-N cross-peak is observed at low ligand/protein molar ratios, resonating at 7.76 (^{1}H) and 120.0 (^{15}N) ppm. The position of the peak shifts downfield in both frequency dimensions, on increasing the concentration of [^{15}N]GCA, towards the frequencies observed for the free molecule (Fig. 1A). An attendant narrowing of the signal indicates that GCA binds the protein and that the line shape of the free ligand becomes dominating in the presence of excess GCA (Fig. 1B). The gradual movement of the peak in subsequent titration steps is consistent with an exchange rate that is higher or similar to the frequency difference between the free and bound signals. The small chemical shift difference between the resonances at the beginning and end of the titration suggests that the ligand amide is exposed to the solvent. Separate signals for the free and bound GCA have never been observed even at lower temperature, similarly to what has been previously found for the interaction of hL-FABP with GCDA.[31] The observation that no further resonances appear along the titration path may suggest that a single ligand molecule is bound to hL-FABP.

Chemical shift perturbation suggests an internal binding for GCA

In order to clarify whether the observed behavior referred to a superficial or internal binding, complementary ^{1}H,^{15}N-HSQC titrations were performed on [^{15}N]hL-FABP:GCA for observation of protein amide signals. Several protein peaks showed perturbations on addition of ligand up to a five-fold excess (Fig. 2A). Higher GCA concentrations did not produce further spectral changes indicating saturation of the binding site(s). A chemical shift perturbation (CSP) analysis was performed by evaluating the residue-specific combined ^{1}H and ^{15}N chemical shift changes observed in the presence and absence of GCA ($\Delta\delta_{HN} = \delta_{HN}^{bound} - \delta_{HN}^{free}$)(Fig. 2B). The sequence-specific backbone resonance assignment of hL-FABP and hL-FABP:GCA was performed according to a standard approach based on analysis of triple resonance CBCA(CO)NH and HNCACB experiments on uniformly [^{15}N,^{13}C]-labeled protein samples, resulting in the identification of 121 (free hL-FABP) and 125 (GCA complex) out of the total 127 residues of the protein. A higher solvent accessibility and decreased stability (see below) prevented full resonance assignment of the unbound protein in the used experimental conditions. Residues showing significant chemical shift changes are outlined in Fig. 2B. The most perturbed region from our analysis is the one corresponding to strand βF. The observation that the amide signals of three internal aromatic residues are affected by binding of ligand represents an indication that GCA is located inside the protein cavity. Additional perturbations are recorded in helix αII and in loop GH (K96 exhibits $\Delta\delta_{HN}$ > 0.5 ppm), possibly reflecting a rearrangement of the protein open end induced by the side chain of a GCA molecule that protrudes towards the solvent.

For comparison purposes, a similar analysis was repeated on hL-FABP bound to oleate (OLA), a known physiological long chain fatty acid ligand. The sequence-specific resonance assignment was here performed because it was published by others[32] only at an advanced stage of this work. After OLA addition several residues, dispersed throughout the polypeptide chain, show large CSP (Fig. 2C). These residues are L9, I29 and G32, the stretch G37-S39, V42, F50, K57, the stretch Q60-F63, T81, V92, I109 and R122. Based on the available structure of hL-FABP:OLA (PDB: 2LKK), several of these CSP can be ascribed to direct binding-induced changes in chemical environment, such as in the case of S39 and R122 whose side chains establish polar contacts with the carboxylate group of the inner OLA (OLA 129) molecule, or F50 and F63 that form the hydrophobic binding surface accommodating the acyl chain of OLA 129. Additional changes located principally in helix αII and strand βD probably reflect indirect conformational changes. It can be noted that F50 and F63 are significantly perturbed after both OLA and GCA addition, again supporting the view that GCA binds inside the protein cavity.

Interaction of GCA with hL-FABP proceeds via a complex pathway

The $^1H,^{15}N$-HSQC titration of GCA into hL-FABP has been further analyzed in detail to obtain information about the binding mechanism. For the vast majority of amide peaks, a single resonance is observed at every titration point, indicating that ligand binding occurs in the fast or intermediate exchange regime. The trace of peak movement along the titration appears linear for most peaks, however in a small number of cases two different directions of movement are observed before and after a ligand/protein ratio of 0.4 (Fig. 2D), indicating that the corresponding residues visit an intermediate chemical environment that differs from that observed at saturation. By inspection of the 1D slices of HSQC cross-peaks it was found that line-broadening affected most of the signals at intermediate titration points, preventing the determination of an affinity constant based on a chemical shift-based binding isotherm.[33] We therefore simulated the observed lineshapes to estimate thermodynamic and kinetic parameters. As an example the experimental ^{15}N lineshapes for the amide signal of residue K121, displaying a linear trajectory of peak movement, are shown in Fig. 2E together with the corresponding simulated lineshapes that best reproduce the data (Fig. 2F). The analysis resulted in an estimated dissociation constant $K_d = 10^{-5}$ M and a dissociation rate $k_{off} = 30\ s^{-1}$, assuming a simple 1:1 binding model. However, it can be noted that the experimental shapes are more complex than expected from simulation. In particular, several shoulders appear in intermediate titration steps that reduce the intensity of peak maxima in comparison with the predicted ones. These complex shapes may indicate the presence of slowly interconverting conformers along the interaction path.

Secondary structure of hL-FABP does not change upon GCA binding

The structure of hL-FABP in the presence of long-chain fatty acid ligands has been shown to be almost completely superimposable with that of the unbound protein both in solution (pairwise backbone RMSD = 1.14 Å between the free protein, PDB: 2L67, and the structure with oleate, PDB: 2L68) and in crystals (pairwise backbone RMSD = 0.56 Å between the free protein, PDB: 3STN, and the one bound to palmitate, PDB: 3STK). Here we collected structural data (HN, HA, CA, CB, CO, N chemical shifts) on the protein backbone for the hL-FABP:GCA complex to ascertain whether the presence of a different ligand scaffold was able to differently shape the protein backbone. The protein φ and ψ backbone torsion angles predicted from chemical shifts using the software TALOS,[34] and the resulting secondary structure elements (Fig. 2B, top), were in agreement with the available structures of hL-FABP indicating that no major structural adaptation is necessary to accommodate GCA.

Intermolecular NOEs show that GCA binds hL-FABP internally

In order to obtain structural information on the ligand binding site and orientation, isotope edited/filtered NMR experiments were performed on a [$^{15}N,^{13}C$]hL-FABP:GCA complex. Resonances of GCA bound to the protein were identified based on *F1*,*F2*-[$^{15}N,^{13}C$]-filtered TOCSY and NOESY (Fig. 3A) experiments starting from a resonance assignment performed on free GCA. A single set of resonances corresponding to bound ligand was observed. Good entry points for assignment were given by the resolved signals of H_N (7.8 ppm, experiments in H_2O), H_{C3} (3.41 ppm), and the three methyl groups (H_{C21}, 0.89 ppm; H_{C19}, 0.82 ppm, H_{C18}, 0.62 ppm) (Fig. 3E). Intermolecular NOE cross-peaks were observed in a *F2*-[$^{15}N,^{13}C$]-filtered NOESY spectrum (Fig. 3B). Due to the severe overlap of signals originated by both GCA and the protein in the spectral region 0-4 ppm, we concentrated on the cleaner portion displaying cross-peaks between protein aromatic side-chains and ligand protons (*F1*: 0-4 ppm, *F2*: 6-8 ppm). The spectral proximity of aromatic proton signals was substantially resolved in constant-time $^1H,^{13}C$ heteronuclear correlation spectra and the assignment exploited intra-residue correlations to the known Cβ chemical shifts in (Hβ)Cβ(CγCδ)Hδ experiments (Fig. 3C) as well as $^1H,^1H$-NOESY spectra. Protein resonances displaying NOE cross-peaks with ligand resonances were thus attributed to the side-chains of F48, F50, and F95. This result is in agreement with the chemical shift perturbation analysis and is consistent with a single binding site.

An established data-driven docking procedure was then used to derive the position of GCA with respect to the protein structure. In this procedure chemical shift perturbation data were introduced as ambiguous (not atom-specific) distance restraints, while NOE data were used unambiguously (Table 1). The computation resulted in the identification of the best cluster of structures with general statistics reported in Table 2. The ligand poses displayed an RMSD of 0.64 Å, showing little variability among the best-scoring solutions (Fig. 4A). The ligand appears well inside the large protein cavity with sterol ring A occupying the bottom of the pocket and the polar glycine residue protruding towards the solvent and occupying the so-called portal region defined by loops CD and EF, and by the helices motif.

Solvent accessibility of amides is similar in GCA- and OLA complexes of hL-FABP

Hydrogen-deuterium exchange (HDX) experiments complement structural studies providing information on solvent accessibility to individual sites and can effectively detect protein dynamic processes occurring over a wide range of time scales (from ms, to hours or days). To measure HDX in real time on hL-FABP and its complexes, lyophilized protein samples bearing protons were dissolved in ^2H_2O and the replacement of amide ^1H atoms by ^2H was monitored from signal intensity decays over time. Very fast 2D $^1H,^{15}N$ heteronuclear correlation spectra were acquired using the band-selective optimized flip-angle short transient (SOFAST) NMR experiments. Representative amide signals decay curves are reported in Fig. S1 of the Supporting Information. It was possible to evaluate exchange rate constants for 33 peaks of unbound hL-FABP, while 26 and 34 peaks were analyzed for the complexes hL-FABP:OLA and hL-FABP:GCA, respectively.

Experimentally determined k_{ex} values were used to calculate residue-specific protection factors $P = k_{int} / k_{ex}$ (reported in Table S1 and mapped on the protein structure in Fig. 5). For the apo protein, the mapping of protection factors suggests that the most stable core is represented by the β strands A, G and J. Helix αI is also partially protected from exchange, while most of the amides in strands D–F and H–I and in helix αII display higher solvent accessibility. Ligand addition perturbs hydrogen exchange along the protein structure, several residues showing increased protection factors in both the OLA- and GCA-bound proteins. In particular helix αI, loop DE and strand βJ appear to be more protected than in the unbound protein. After addition of OLA, helix αII is partially stabilized and also most residues in strands βA, βC, βH and βI show reduced exchange. In the complex with GCA, helix αII is still quite solvent accessible, while residues in strands βC, βG, βH, and βI experience significant increase in their protection factor values. It appears that OLA binding has a stronger protection effect on residues in strands βH and βI, while binding of GCA determines higher quenching of exchange in strand βC.

From the observation of the pH dependence of k_{ex} (Fig. S2) we found that the intrinsic exchange rates fell within the bimolecular EX2 regime, allowing the determination (see Experimental Section) of ΔG_{unf} = 6.70 kcal mol^{-1} for unbound hL-FABP, ΔG_{unf} = 8.75 kcal mol^{-1} for hL-FABP:OLA and ΔG_{unf} = 8.13 kcal mol^{-1} for hL-FABP:GCA, concluding that the addition of fatty acid and bile acid determines a similar increased protein stability.

Fast-exchanging protons which escape real time HDX measurements were detected in water-protein magnetization transfer experiments (CLEANEX-PM). Amide resonances with positive intensity in CLEANEX-PM experiments recorded with 75 ms mixing time were identified and mapped on the three-dimensional structure of hL-FABP (Fig. 5). In the unbound protein, fast-exchanging amidic groups belong to residues located in helix αII, strands βA, βB, βE, loops A-αI, αII-B, CD, EF, HI, IJ. After the addition of ligands, a number of residues experience decrease of proton exchange, mainly located in the αII-βB, CD, and EF regions. Fast-exchanging amides appear in the bound proteins in loop FG, and for the GCA-bound protein also in strand βH. No further significant differences are found between hL-FABP:OLA and hL-FABP:GCA, indicating that the H-bond network of protein backbone amides is essentially unchanged.

Amide nuclear spin relaxation and fast dynamics of hL-FABP complexes

Protein motions in the ps-ns timescale are conveniently identified by measuring nuclear spin relaxation. Longitudinal ^{15}N R_1 and transverse ^{15}N R_2 relaxation rates and the {^{1}H}-^{15}N heteronuclear nuclear Overhauser effect (*hnNOE*) encapsulate different combinations of internal motions.[35] Interpretation of relaxation in terms of the underlying physical processes requires further processing and modeling of data,[35] however a simple phenomenological interpretation of unprocessed R_1, R_2, and *hnNOE* is appropriate for identifying site-specific differences in dynamics between bound and unbound hL-FABP. Furthermore, an accurate determination of order parameters may be impaired by significant contributions of chemical exchange to transverse relaxation. Relaxation data were measured on ^{15}N-enriched hL-FABP, hL-FABP:OLA, and hL-FABP:GCA. Resonances of low intensity and those showing overlap were excluded from the analysis. R_1 average values were found almost identical for all the three systems and the dispersion of values around the average was small (Fig. 6): 1.34 ± 0.062 s^{-1} (hL-FABP), 1.39 ± 0.068 s^{-1} (hL-FABP:OLA), and 1.36 ± 0.064 s^{-1} (hL-FABP:GCA). Changes in hL-FABP R_1 larger than 10% on addition of OLA were observed for residues F15, E27, F48, T51, N61, V83, G87, I109, and I127 which are scattered over the protein structure, while addition of GCA produced changes >10% only in residues V38, F48, and I109. The absence of significant decrease in R_1 values from the average suggests that ps-ns flexibility is quite limited for both the unbound and the ligand bound proteins.

Fast dynamics is however best detected from *hnNOE* data, which are plotted in Fig. 6 for the three protein systems. Most residues involved in secondary structure elements display *hnNOE* close to 0.8 as expected for rigid amide atoms, however average values of 0.77 ± 0.035 (hL-FABP), 0.79 ± 0.03 (hL-FABP:OLA), 0.78 ± 0.028 (hL-FABP:GCA) denote the presence of regions of higher local mobility. In the free protein the most flexible segments are helix αII, loops αII-B, part of strands βC and βD, loops CD and EF. Addition of ligands partially reduces this mobility, particularly in loop CD, strands βC and βD and helix αII to similar extent for OLA and GCA. Loop αII-B appears to maintain higher flexibility in the presence of GCA than with OLA. Among the residues showing lowest *hnNOE* (~0.6) in the unbound protein, N61 and E77 become rigidified in the presence of both the fatty- and the bile acid, while G87 remains highly mobile in the bound proteins. F63 displays high mobility in the presence of GCA but not of OLA.

Anisotropic tumbling contributions to R2 are negligibly small in the two complexes

R_2 relaxation rates are as well affected by ps-ns backbone mobility, however they are also highly dependent on anisotropic molecular rotation and chemical exchange. Effects of anisotropic motion can be identified by several approaches, including the magnetic field dependence of relaxation rates or simply from the comparison of experimental residue-specific R_2/R_1 values with those predicted on the basis of structural coordinates assuming a completely rigid molecule. Rotational diffusion tensor parameters calculated with HYDRONMR[36] on the structure of hL-FABP (PDB: 2L67) indicate a small anisotropy (anisotropy, ξ = 1.18, rhombicity, η = 0.21) and this feature is preserved when the cavity is occupied by ligands (hL-FABP:OLA, PDB: 2L68, ξ = 1.15, rhombicity, η = 0.37). This result is reflected by a small oscillation of predicted R_2/R_1 values around the average (Fig. S3), indicating that high R_2 values are suggestive of chemical exchange occurring at a slower rate than rotational tumbling.

Slow motions are increased upon binding of GCA

In hL-FABP, residues displaying R_2 values higher than the mean plus one standard deviation (11.00 ± 0.78 s^{-1}) are: Q8, Q30, H47, T51, T53, Q60, E62, S100, T102, T110, T112, L115, K121, and R126. On addition of OLA the mean R_2 is almost unchanged (11.07 ± 0.82s^{-1}) and residues displaying deviations from the average are: I22, I29, K33, H47, F50-I52, K57, E62, F63, V65, V79, T93, K99-V102, M113, and K121. The largest transverse relaxation rates within the bound protein are observed for residues I22, K57, V79, and S100, which display significantly lower values in the unbound protein. The average R_2 rate of 11.34 ± 1.60 s^{-1} in hL-FABP:GCA indicates increased contributions of μs-ms timescale motions in this complex compared to both the unbound and the OLA-bound protein (Fig. 6). Residues Q8, N14, K20, L24, E26, I29, G32, V38-E40, F50, T51, I59, E62, E72, T73, T75, V79, K80, F95, S100, V101, I109, and M113 exhibit R_2 values higher than the average. The largest rates are observed for residues Q8, N14, K20, L24, E40, F50, T51, I59, E62, E72, T75, V79, K80, F95, S100, and V101, essentially belonging to an imaginary belt crossing β-strands A-H or located at the through-space contact between loop EF and the inter-helix loop. Most of these residues display close-to-average values in the unbound protein. These data indicate that conformational exchange contributions to R_2 in hL-FABP are slightly increased in the presence of OLA and significantly increased on addition of GCA.

The indication obtained from the analysis of ^{15}N R_2 that chemical exchange occurs in hL-FABP and in its bound states prompted us to perform a more detailed analysis using Carr-Purcell Meiboom-Gill relaxation dispersion (CPMG RD) experiments. CPMG RD NMR detects processes occurring in the intermediate-fast regime ($k_{ex} \approx \Delta v$) resulting in enhanced relaxation rates $R_2^{obs} = R_2^0 + R_{ex}$, provided that there is significant chemical shit difference among exchanging states.[37] The dependence of ^{15}N transverse relaxation rates on the strength of an applied radio frequency spin-lock (v_{CPMG}) was evaluated site-specifically for hL-FABP free and in complex with either GCA or OLA. Representative dispersion curves are shown in Fig. 7. The amount of exchange broadening can be estimated from the height of the dispersion curve, $\Delta R_2^{obs} \approx R_{ex} = R_2^{obs}$ (ν_{CPMG}^{0}) - R_2^{obs} (ν_{CPMG}^{∞}), and the measured values are displayed along the protein sequence in Fig. 7. In hL-FABP, ΔR_2^{obs} values above 4 s^{-1} are observed for residues belonging to all β-strands except βE and βF. Strands βC and βD display extremely high exchange contributions to R_2. The median ΔR_2^{obs} decreases from 2.49 s^{-1} to 2.02 s^{-1} on addition of OLA. Particularly noteworthy is the reduction of values corresponding to residues F50, T51, E62, F63: the two phenylalanine side chains contribute to form the binding site of OLA129, the internal oleate ligand, based on the structure of hL-FABP:OLA (PDB: 2LKK). On the contrary, the loops connected to helix αII experience increased exchange broadening together with K57, all positioned in proximity of OLA128, the superficial oleate ligand. The interaction of hL-FABP with GCA produces significant perturbations in terms of µs-ms dynamics over the whole protein structure, as denoted by a largely increased median ΔR_2^{obs} of 6.1 s^{-1}, indicating a ligand-specific dynamic behavior of the protein backbone.

Two-state exchange model for h-LFABP:OLA and hL-FABP:GCA complexes

CPMG RD data can also be analyzed in greater detail to extract kinetic (k_{ex}), thermodynamic (P_A, population of state A), and structural information ($\Delta\omega$, chemical shift difference between the exchanging states A and B) on conformational equilibria. Assuming a simple two-state exchange model, dispersion curves can be fitted using known equations (see Materials and Methods). An average individual exchange constant of 536 ± 391 s^{-1} was determined for 37 residues of unbound hL-FABP displaying non-flat dispersion curves. Slow kinetic rates ($k_{ex} < 100$ s^{-1}) were determined for residues T53, N61, and F63, while K36, Q60, T75, and V83 displayed $k_{ex} > 900$ s^{-1}, possibly indicating that the protein is visiting additional excited states. Sixteen residues displayed fast-limit exchange while 21 appeared to undergo slow-limit exchange with an excited-state population $P_B = 0.28 \pm 0.056$ and an average chemical shift difference of 0.79 ± 0.73 ppm. On addition of OLA, the average exchange rate calculated for 40 residues increases to 1129 ± 583 s^{-1}, and twelve dispersion curves classified in the slow-limit regime are fitted by $P_B = 0.27 \pm 0.11$ and $\Delta\omega = 1.08 \pm 0.91$ ppm, indicating an accessible excited conformational state with significant local structural differences compared to the ground state. For hL-FABP:GCA 70 non-flat curves were fitted, resulting in $k_{ex} = 594 \pm 554$ s^{-1}, with Q10, V38, E62, K20, L24, S56, N61, T73, and K80 displaying $k_{ex} < 100$ s^{-1} and I22, V38, E62, V83, V101, T102, K121, and R126 exhibiting $k_{ex} > 900$ s^{-1}. Thirty-five residues appeared to undergo exchange in the slow regime with an excited state of population $P_B = 0.23 \pm 0.095$ and with an average chemical shift difference between states of 1.46 ± 0.95 ppm, the largest observed being 3.35 ppm (L24).

Discussion

In this work we provide a definitive demonstration that hL-FABP is able to bind bile salts. Titration data monitored by NMR observation of either ligand or protein provided the indication that a single molecule of GCA specifically interacts with the protein. In accord with a significant number of structural studies performed on iLBPs, the presence of ligands inside the large internal pocket does not induce extensive conformational rearrangements. When bound to GCA, hL-FABP preserves the secondary structure elements of the unbound protein, as derived from chemical shift data. The network of hydrogen bonds does not appear strongly perturbed as well, considering that all amide protons known to be involved in this type of interaction in the structure of unbound hL-FABP display small HDX rates in the hL-FABP:GCA complex. Fast-exchanging protons identified from CLEANEX measurements appear in similar numbers in unbound hL-FABP and its complexes with either OLA or GCA, and are not surprisingly mainly localized in loop regions. A general increase in HDX-derived protection factors is however determined after addition of OLA and GCA, indicating an increased protein stability. By comparison with related proteins, it can be concluded that the scaffold of iLBPs is pre-formed to allow accommodation of ligands without the need of major structural adaptation between the unbound and ligand-saturated states, but with a favorable energetics derived from the formation of a stable hydrophobic core contributed by the ligand(s).

Intermolecular distance constraints obtained from *F1*,*F2*-[^{15}N,^{13}C]-filtered NOESY spectra, together with CSP data, were sufficient to reliably determine a location of the bile salt in the protein interior using an established data-driven docking approach. The steroid nucleus of GCA occupies a region that mostly overlaps with the binding site of the internal oleate molecule, OLA129. The bile salt side chain extends towards the binding site of OLA128, however alternative conformations to that calculated with HADDOCK seem possible due to the elevated number of rotatable dihedral angles. Thus, while the shape or physico-chemical properties of the protein cavity are not compatible with a simultaneous occupation by two glyco-conjugated tri-hydroxy bile salt molecules, it cannot be excluded that a heterotypic complex can be formed, where both a bile salt and a LCFA are present. The binding of a single bile salt molecule is further distinctive from the 1:2 stoichiometry observed for BABPs, the phylogenetically closest FABPs. Binding occurs with strong positive cooperativity in cL-BABP and hI-BABP resulting in an overall K_d falling in the nanomolar range, signifying the need to effectively sequester potentially cytotoxic molecules from the cytosol.[38,39] For GCA binding to hL-FABP we have estimated a K_d of about 10 µM. This finding then opens the question about how mammalian hepatocytes can be protected against high concentration levels of bile salts. An intriguing possibility is that cooperative mechanisms are established in the presence of complexes with a mixed lipid cargo. In this line, heterotypic complexes formed by hI-BABP and cI-BABP with two different bile salt molecules have been the subject of study of recent publications.[40,41]

Whether a single or two molecules of ligand are involved, interactions with iLBPs appear in general not to occur in discrete concerted binding events, rather through complex binding pathways involving several excited states.[42–44] In this work we observed for hL-FABP complex HSQC cross-peak line shapes characterized by several shoulders, consistent with the presence of slowly exchanging intermediate conformers along the titration path. Furthermore, few peaks displayed two different directions of movement before and after a ligand/protein ratio of 0.4, also suggestive of an intermediate bound state. These findings may reflect the presence of both off-path intermediates as well as productive long-lived bound conformers. Further investigations are required to assess whether these complexity of the bile salt interaction with hL-FABP masks a possible route for ligand entry and egress.

The latter is indeed the major unresolved question about ligand binding to iLBPs. An early theory derived from pioneering studies on rI-FABP, and dubbed the ‘dynamical portal hypothesis’, explained ligand internalization to be possible thanks to a significant flexibility of residues belonging to helix αII and turns CD and EF (the portal).[45] However for a number of iLBPs, including H-FABP, E-FABP, and I-BABP, a substantial rigidity, in the ps-ns time scale, of the protein backbone was assessed.[46,47] In a more recent work on rI-FABP, the absence of significant fast time scale motions was observed in both the free and bound states.[48] A comparison of the backbone dynamics of hL-FABP alone and in complex with OLA has been described previously in terms of generalized order parameters obtained from a model-free analysis of NMR relaxation data, concluding that ligand binding restricts fast motions of the portal and gap (βD-βE and βF-βG) regions.[12] Our analysis of $\{^{1}H\}$-^{15}N NOE data substantially confirms these results but highlights that only minor changes in fast motions occur on addition of either OLA or GCA. The conclusion can be drawn that ligand binding to FABPs does not significantly affect fast time scale motions experienced by backbone amides and that functional dynamics may occur in a slower regime.

A previous study assayed to correlate the μs-ms dynamics of hL-FABP with the entry/exit process of the exogenous ligand ANS, but a clear dynamics-function relationship could not be established.[49] The conformational exchange experienced by the unbound protein was interpreted with the intrinsic tendency of hL-FABP to access a bound-state conformation even in the absence of the ligands, in agreement with previous work on cL-BABP.[44]

The here reported comparison of protein slow dynamics indicates that, at variance with the behavior observed for other proteins of the family, ligand binding does not quench slow motions. CPMG RD experiments, reported for CRBP-I and –II, revealed that the high percentage of residues showing detectable conformational exchange on a μs-ms time scale in the unbound form was substantially quenched upon retinol binding.[50] Analogously, in hI-BABP, residues found to undergo a conformational exchange process in the unbound protein (nearly 25%) exhibited a flat relaxation in the doubly ligated complex.[40] The analysis of relaxation profiles shows that 37 and 40, out of the 127 hL-FABP residues, are involved in dynamic exchange in the unbound protein and the oleate complex, respectively, while up to 70 residues exhibited non-flat curves in the GCA complex. Experimental ΔR_2^{obs} values clearly evidence that partial occupation by GCA of the available space in the large internal pocket substantially increases conformational dynamics of the entire protein. Interestingly, the only residues showing decreased mobility do not display CSP effects upon GCA addition. When this comparison is extended to the oleate complex, an increased flexibility is observed for few residues, all located in loops, while a partial quench of CPMG amplitudes is observed for residues in loop αII-βB and strands βC, βD, and βG, in agreement with H/D exchange data reflecting the formation of stable H-bonds on the C-terminal face of the barrel.

Global data analyses of relaxation dispersion curves are reported in Tables S2-4. Interestingly, in the unbound protein, residues displaying the highest exchange rates (Fig. S4), are also among those experiencing highest CSP upon OLA (K36, Q60) and GCA addition (T75). These data suggest that dynamics of the unbound protein accounts for its functional capability to sequester both fatty- and bile acids. In this line it is worth noting that the exchange rates increase for the doubly ligated OLA complex for a group of residues located at the opening of the portal entrance which are also involved in GCA binding. Thus the protein undergoes μs-ms dynamics not only in the unbound but also in the bound form, affecting residues competent for binding of both ligands. hL-FABP appears to visit excited states that can be captured by different types of ligands, substantiating a functional correlation between dynamics and promiscuous binding.

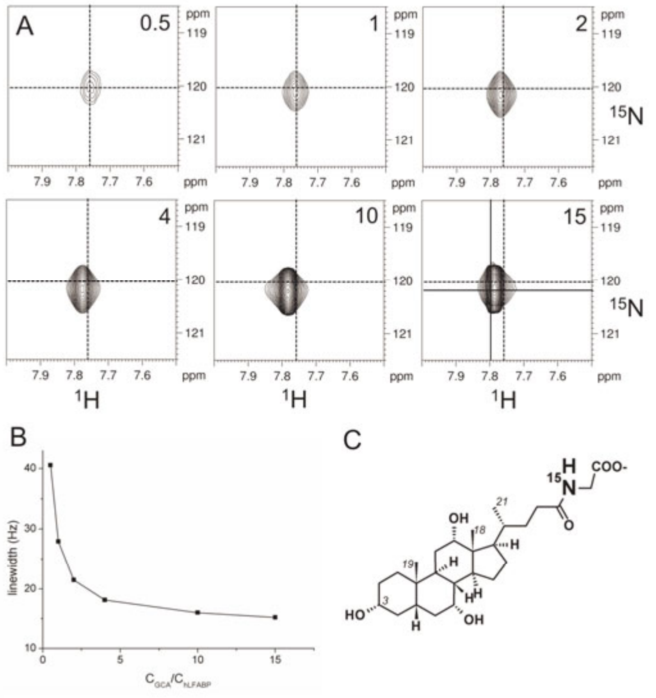

Figure 1. Ligand-observed ^{1}H,^{15}N-HSQC NMR titration of hL-FABP with [^{15}N]-GCA. A) Contour plots of portions of spectra showing the single observed HN resonance of GCA on increasing ligand/protein molar ratios (reported on the top-right of each sub-panel). The two-dimensional chemical shift position of the peak in the lowest recorded ligand/protein ratio is marked by dotted vertical and horizontal lines in all sub-panels. Solid lines mark the position of the HN resonances observed for the unbound GCA. B) Plot of the ^{1}H linewidth of the HN HSQC cross-peak observed along the titration. C) Structural formula of GCA. The ^{15}N-enrichment is indicated. The numbering of selected carbon atoms is displayed.

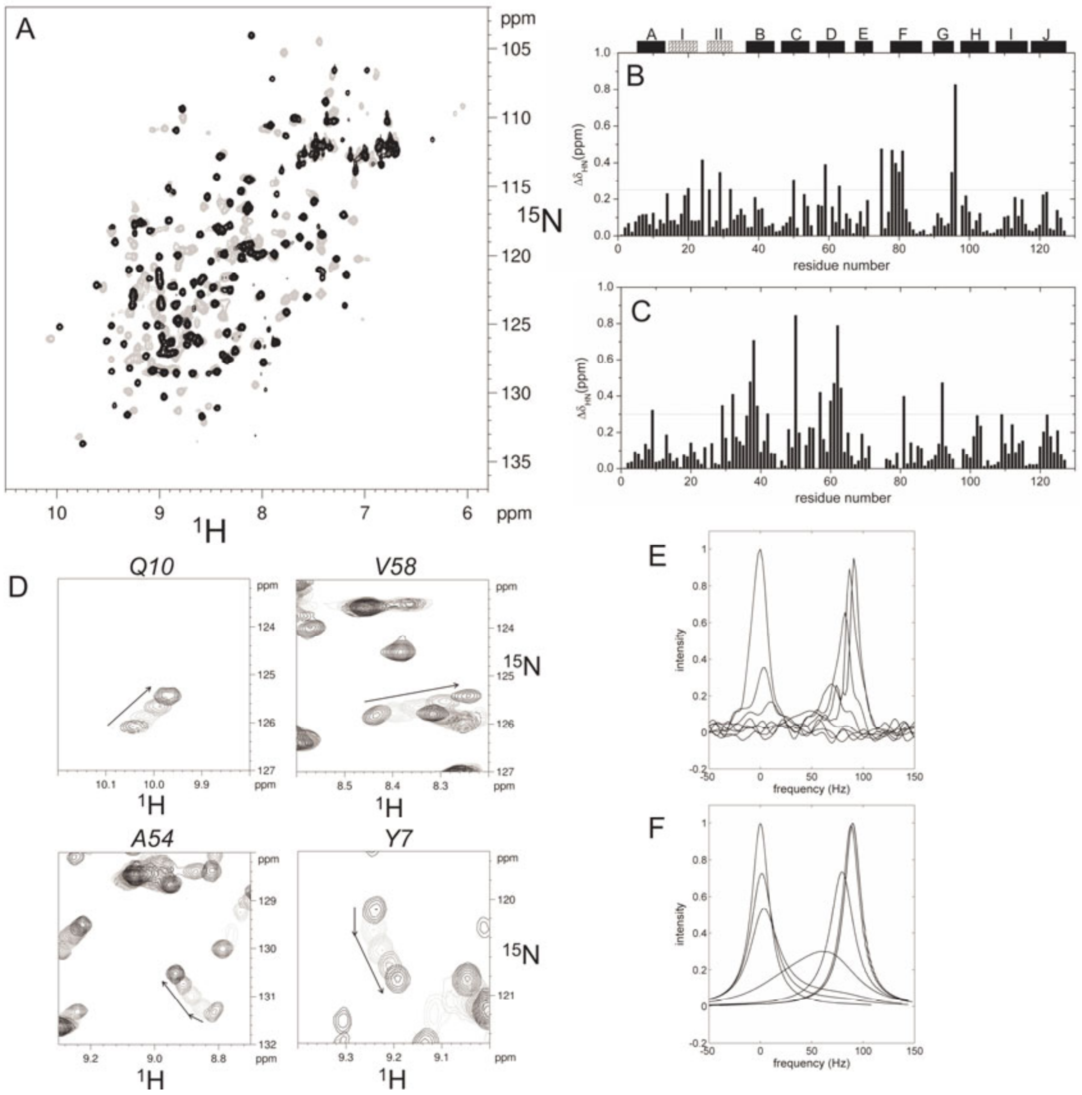

Figure 2. Protein-observed ^{1}H,^{15}N-HSQC NMR titration of [^{15}N]-hL-FABP with GCA. A) Overlaid spectra of unbound hL-FABP (grey) and hL-FABP:GCA in a protein:ligand ratio of 1:5 (black). B) Combined H,N chemical shift difference $\Delta\delta_{HN}$ between GCA:bound and unbound hL-FABP. The dotted line corresponds to the average value plus one standard deviation. Residues showing $\Delta\delta_{HN} \geq 0.25$ ppm are K20, L24, E26, I29, G32, F50, I59, F63, T75, the stretch K78-T81, F95 and K96. C) Combined H,N chemical shift difference $\Delta\delta_{HN}$ between OLA:bound and unbound hL-FABP. The dotted line corresponds to the average value plus one standard deviation. Residues showing $\Delta\delta_{HN} \geq 0.3$ppm are L9, I29 and G32, the stretch G37-S39, V42, F50, K57, the stretch Q60-F63, T81, V92, I109 and R122. D) Peak trajectories along the titration of hL-FABP with GCA for residues Q10, V58, A54, and Y7. E) ^{15}N experimental lineshapes for residue 121 observed at titration points: 0 (0 Hz), 0.1, 0.2, 0.6, 1.0, 1.8, and 5.0 (90 Hz from initial point) ligand/protein molar ratios. F) Simulated lineshapes for peak displayed in E, obtained using $K_d = 10^{-5}$ M and $k_{off} = 30\ s^{-1}$ in a 1:1 binding model.

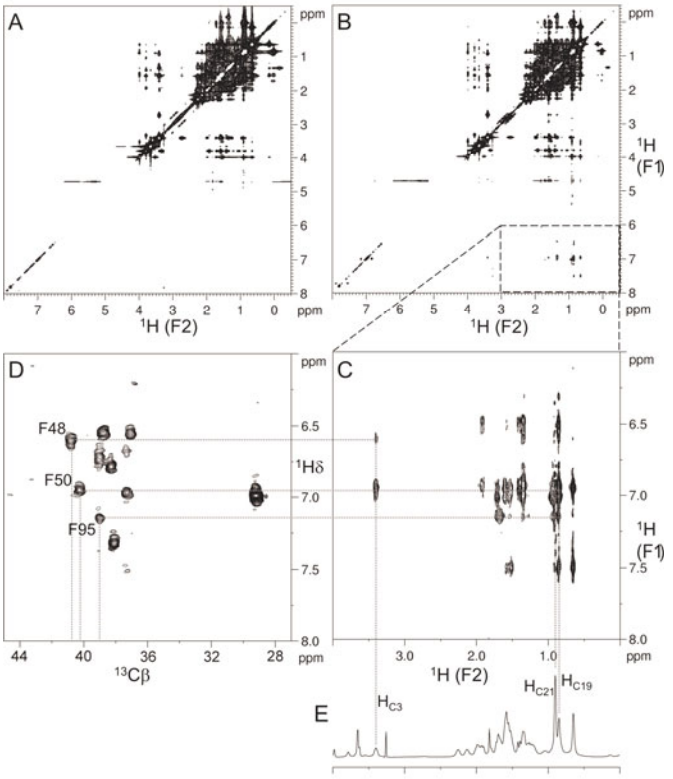

Figure 3. Identification of intermolecular NOE cross-peaks for the complex hL-FABP:GCA. A) $F1$,$F2$-[^{15}N,^{13}C]-filtered NOESY spectrum for observation of ligand resonances and intra-ligand NOEs. B) $F2$-[^{15}N,^{13}C]-filtered NOESY spectrum for observation of protein-ligand NOEs. C) Enlarged view of portion of B showing intermolecular NOEs between protein aromatic side-chains and ligand resonances. D) (Hβ)Cβ(CγCδ)Hδ correlation spectrum for assignment of aromatic side-chain proton resonances. E) Portion of ^{1}H spectrum of GCA. The assignment of selected intermolecular NOE cross-peaks is indicated by dotted lines, the corresponding protein residues being labeled in D and ligand atoms in E. The spectra of the complex were acquired on a sample containing a five-fold excess of ligand.

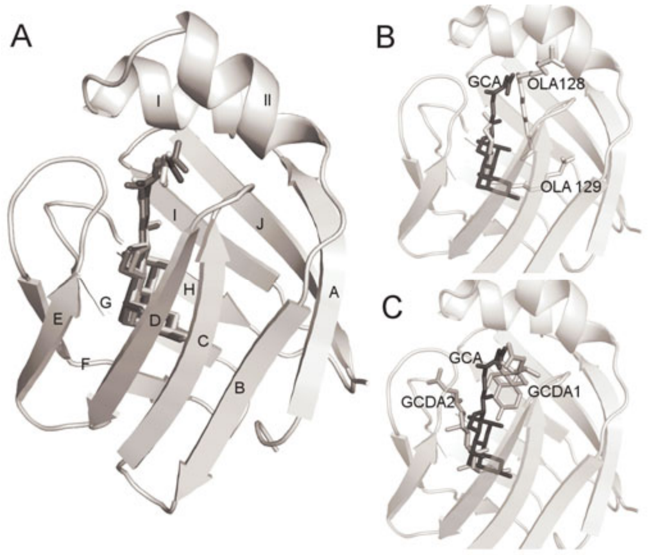

Figure 4. Structural model of the hL-FABP:GCA complex. A) HADDOCK structural model, the four ligand conformations of the best docking cluster are displayed. B) Comparison of ligand binding sites and conformations between hL-FABP:GCA (this work) and hL-FABP:OLA (PDB: 2LKK). C) Comparison of ligand binding sites and conformations between hL-FABP:GCA (this work) and chicken L-BABP:GCDA (PDB: 2JN3). The protein backbone of hL-FABP is in cartoon representation, ligands are depicted in sticks, GCA in hL-FABP is represented in dark grey, OLA in hL-FABP and GCDA in chicken L-BABP are displayed in light grey. The protein structures of hL-FABP:OLA and cL-BABP:GCDA were best superimposed to that of hL-FABP:GCA and are not shown for clarity.

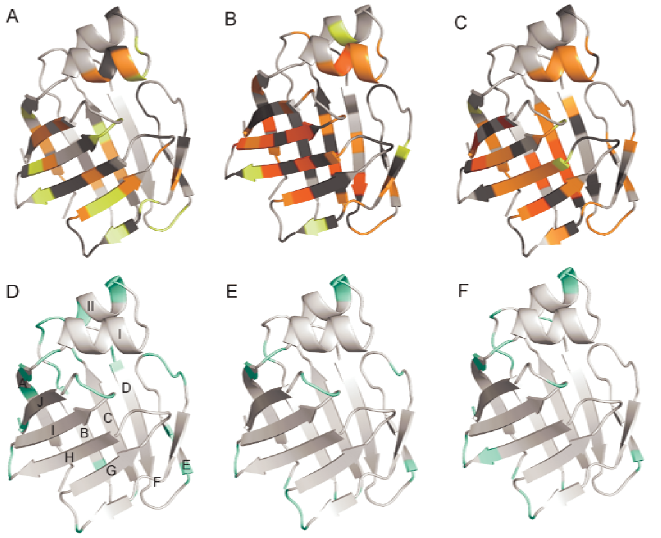

Figure 5. Hydrogen exchange analysis for the protein in its unbound and complexed forms. Protection factors measured from real time HDX experiments on A) hL-FABP, B) hL-FABP:OLA, C) hL-FABP:GCA are mapped on the protein structure with the following color code: light grey $P < 10^3$, yellow $10^3 < P < 10^4$, orange $10^4 < P < 10^7$. Amide residues showing no signal decay in 24 h are colored in red and are the following: Y7, M19, F63, V101, E103, T110, M113 and F120 (OLA complex), I41, V42, F48, F50, F120 and S124 (GCA complex), K49, L91 and I109 (both complexes). Residues that could not be analyzed are indicated in dark grey. Fast-exchanging amides detected in CLEANEX-PM experiments performed on D) hL-FABP, E) hL-FABP:OLA, F) hL-FABP:GCA are colored in cyan. Secondary structure elements are labeled in D).

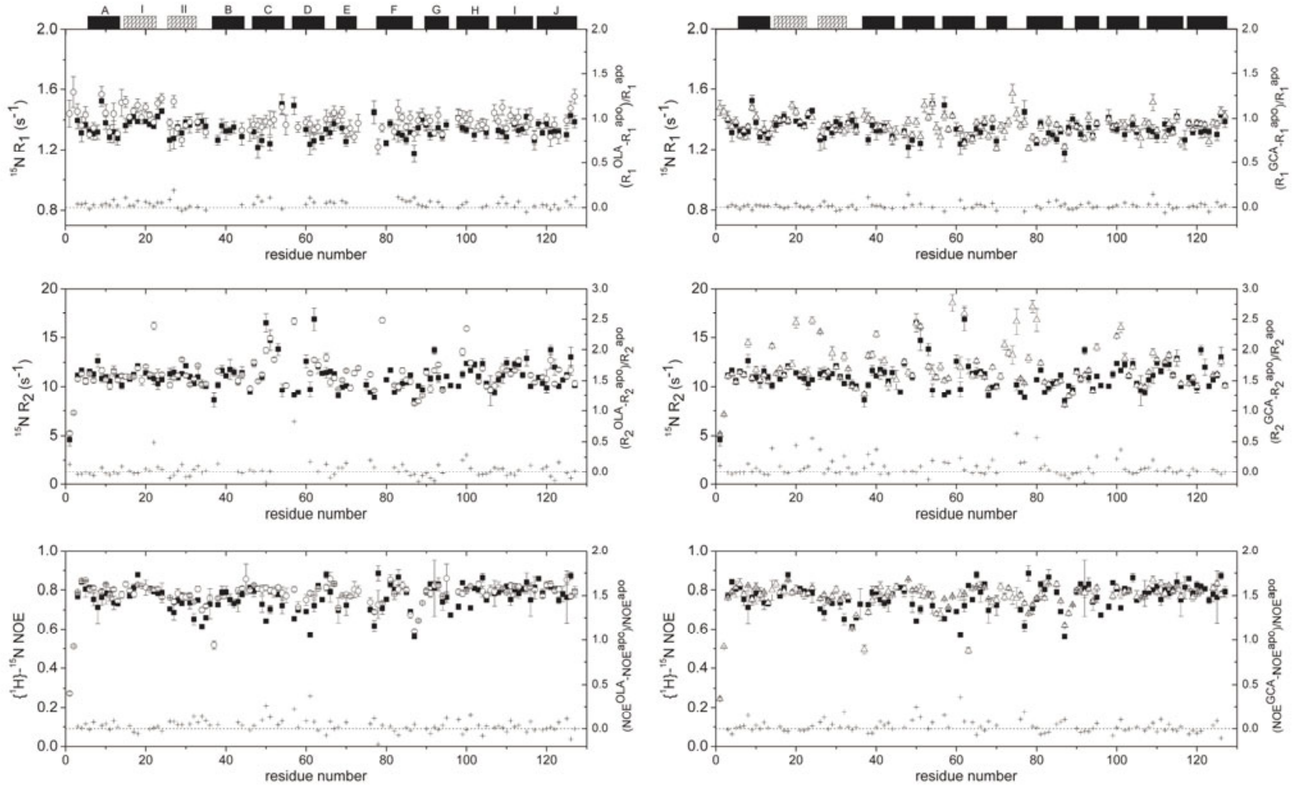

Figure 6. Plot of ^{15}N longitudinal (R_1) and transverse (R_2) relaxation rates and {^{1}H}-^{15}N NOE versus amino acid sequence. For each plot, the values for the apo protein are represented by black filled squares, while the values for the protein in complex with OLA and GCA are represented by empty circles (left panels) and empty triangles (right panels), respectively. The right scales refer to normalized differences of values reported on the left scales. Secondary structure elements corresponding to ligand bound proteins are reported on top: β sheets are represented by black boxes and α-helices by shaded boxes. Unassigned amide resonances are: F50, I52, S56, I59, F63, L71, E72, T73, M74, N97 (hL-FABP); M74, T75, K80, K96, N97 (hL-FABP:OLA); Q60, N97 (hL-FABP:GCA). Otherwise missing values refer to data that were removed due to poor signal/noise or overlap of the corresponding resonances.

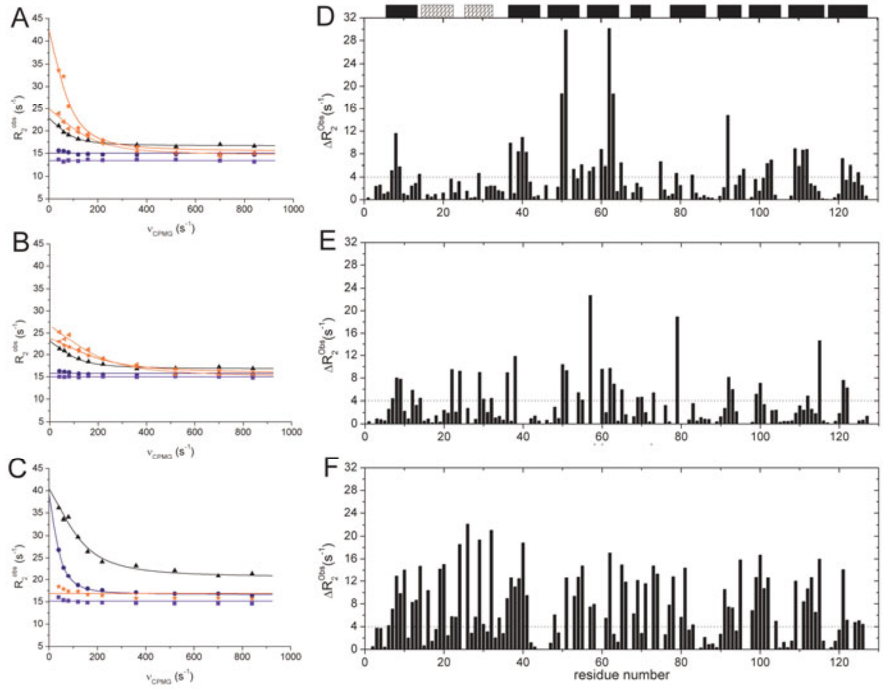

Figure 7. Carr-Purcell Meiboom-Gill (CPMG) transverse relaxation rate dispersion. A-C) R_2 dispersion curves as a function of applied CPMG field strength for representative amino acid residues in hL-FABP (A), hL-FABP:OLA (B), hL-FABP:GCA (C). F63 (red stars) displayed slow-limit exchange in A, fast exchange in B, and no exchange in C. Q60 (orange triangles) displayed fast exchange in A, slow exchange in B, and could not be measured accurately in C); E14 (black triangles) was in fast exchange in all cases; E16 (dark blue filled circles) was not exchanging in A and B and was in fast exchange in C; A17 (blue filled squares) displayed no chemical exchange in all samples. Continuous lines correspond to best-fit curves. D-F) Exchange contribution to transverse relaxation rate plotted along the protein sequence for hL-FABP (C), hL-FABP:OLA (D), hL-FABP:GCA (F) and estimated as ΔR_2^{obs}=R_2(40 s^{-1})-R_2(840 s^{-1}), corresponding to the first and last point of the dispersion curve. A threshold for exchange of 4 s^{-1} is indicated by a dotted line.

Table 1. Interaction restraints used for the calculation of the adduct of hL-FABP with GCA within Haddock.

Protein residues	Ligand atoms
K20 (CSP)[a]	all
L24 (CSP)	all
E26 (CSP)	all
I29 (CSP)	all
G32 (CSP)	all
I59 (CSP)	all
T75(CSP)	all
K78 (CSP)	all
V79 (CSP)	all
K80 (CSP)	all
T81 (CSP)	all
F95 (CSP)	all
K96 (CSP)	all
Cδ F48 (NOE)[b]	C_3
Cδ F50 (NOE)	C_3
Cδ F50 (NOE)	C_{19}
Cδ F95 (NOE)	C_{19}
Cδ F95 (NOE)	C_{21}

In parentheses the experimental methods used to define the restraint are reported. [a] CSP: chemical shift perturbation data. [b] NOE information derived from F_2-[^{15}N,^{13}C]-filtered NOESY experiment.

Table 2. Structural statistics of the cluster of models of hL-FABP in complex with GCA showing lowest Haddock score.

Intermolecular energies after water refinement[a]	
E_{vdw} (kcal mol^{-1})	-25.95
E_{elec} (kcal mol^{-1})	-57.28
Haddock scores (kcal mol^{-1})	-44.58
Average RMSD on protein backbone interface[b] (Å)	0.58 ± 0.29
Average RMSD on ligand interface[b] (Å)	0.64 ± 0.10

[a] The energies values refer to the four best models of the evaluated cluster. [b] The average Root Mean Square Deviation values were calculated after protein backbone fitting using all the models of the best cluster.

Experimental Section

Recombinant protein sample preparation

The gene encoding for the hL-FABP was cloned into pQE50 vector between BamHI and HindIII restriction enzymes. For cloning purposes four residues were added at the N- and C-terminus of the protein sequence, MRGS and LVPR respectively. The plasmid encoding for hL-FABP was then transformed into *E. coli* SG (Qiagen) cells used as the host strain for the protein expression. Luria-Bertani (LB hereafter) broth or M9 minimal medium, supplemented with 1 g/l $^{15}NH_4Cl$ or $^{15}NH_4Cl$ and 4 g/l ^{13}C-labelled glucose as nitrogen and carbon sources, were used to obtain unlabelled and ^{15}N- or ^{15}N,^{13}C-labelled protein, respectively. Protein expression and purification was achieved as elsewhere indicated.[51] Protein delipidation from endogenous lipids was obtained by chromatographic separation in a Lipidex column at 37 °C.[52] The purity of the protein was checked by SDS-PAGE in 15% polyacrylamide gels. All the samples were prepared in 10 mM phosphate buffer, pH 6.5, containing 0.02% NaN_3 and 7% ^2H_2O unless differently indicated. The final concentration of the protein was determined by UV-spectroscopy, measuring the OD_{280}.

Protein-ligand NMR titration experiments

Unlabelled sodium glycocholate (GCA) and sodium oleate (OLA) were purchased from Sigma. ^{15}N-enriched GCA was prepared as described elsewhere.[23] For a protein-observed titration with GCA, ^{1}H,^{15}N-HSQC spectra were recorded on [^{15}N]hL-FABP containing increasing amounts of bile salt in ligand/protein molar ratios of 0.1, 0.2, 0.4, 0.6, 0.8, 1, 1.8, 2.3, 3.5, 5, and 10. A different protein sample was directly presented with OLA at a final ligand/protein ratio of 2.5. The ligand-observed titration points were collected at the same GCA/protein molar ratios specified above.

NMR experiments were run on a Bruker Avance III 600 spectrometer, operating at 600.13 MHz proton Larmor frequency, equipped with a triple resonance TCI cryoprobe, incorporating gradients in the z-axis. ^{1}H,^{15}N-HSQC spectra were acquired with 8-64 transients, spectral windows of 12 ppm in the ^{1}H and 36 ppm in the ^{15}N frequency dimensions, collecting 256 t_1 increments, each consisting of 2048 complex points. Water suppression was achieved with gradient coherence selection. All experiments were acquired at 25 °C.

NMR experiments for resonance assignment and collection of distance information

Standard triple resonance experiments, HNCA, HN(CO)CA, HNCACB, CBCA(CO)NH, HNCO, and ^{15}N HSQC-NOESY (100 ms mixing time) were recorded at 25 °C on ^{15}N,^{13}C- labeled samples to achieve backbone atoms assignment of hL-FABP in its unbound form and in complex with oleate or GCA.

The chemical shift perturbation for each amide resonance observed between bound and unbound protein states has been calculated using the following expression: $\Delta\delta_{HN} = [(\Delta\delta_H)^2+(\Delta\delta_N/5)^2]^{1/2}$, where $\Delta\delta_H$ and $\Delta\delta_N$ are the chemical shift changes (for ^{1}H and ^{15}N, respectively) observed upon the addition of the ligands.

In order to detect intermolecular NOEs for the hL-FABP:GCA complex, 2D [^{15}N,^{13}C]-filtered NOESY experiments were performed on samples containing ^{15}N,^{13}C-labeled protein and unlabeled ligand, in 98% ^2H_2O. A mixing time of 100 ms, a recycle delay of 1.2 s, 12 ppm spectral windows in both dimensions, and 576 points in the F_1 dimension were employed. A frequency-swept adiabatic inversion pulse of 1.75 ms (at a power level of 11.17 dB) with a 10.5 kHz sweep frequency centered at 70 ppm was employed to purge signals of protons bound to ^{13}C. The WATERGATE pulse scheme was used for water signal suppression.

Hydrogen exchange experiments

Hydrogen/deuterium exchange (HDX) experiments were performed at $p^2H = 7.4$ for free hL-FABP and in complex with GCA and $p^2H = 7.8$ for the protein in complex with OLA. ($p^2H = pH_{read} + 0.4$). In order to verify the exchange regime (bimolecular or unimolecular), experiments were performed also at $p^2H = 6.4$. The samples were prepared by dissolving 5 mg of delipidated and lyophilized [^{1}H,^{15}N]hL-FABP in 600 µl of 10 mM Na_2HPO_4/NaH_2PO_4 buffer in ^2H_2O. For experiments with the complexes, the protein was lyophilized in the presence of either excess of GCA or OLA. The final protein concentrations were ~0.5 mM. The solutions were briefly centrifuged at 4 °C to remove insoluble debris and transferred into 5 mm NMR tubes. The exchange behavior of the different samples was followed by the acquisition of a series of SOFAST-HMQC NMR experiments[53] collected with 700 points in F_2 and 192 complex data points in F_1, using a relaxation delay of 0.5 s with 2 scans. The band-selective ^{1}H excitation (PC9) and refocusing (RSNOB) pulses were characterized by pulse lengths of 2.33 and 0.817 ms, respectively. HDX rate constants were determined by fitting cross-peak volumes to a first-order exponential decay:

$$I(t) = I(0)e^{-k_{ex}t}$$

where $I(t)$ represents the volume of the cross-peaks at the time point t, $I(0)$ the volume of the cross peaks at t = 0 corresponding to 12 min for all the samples; k_{ex} is the observed rate of hydrogen exchange and t is the time in minutes. Exponential decays were fitted with the program Sigmaplot (Jandel Scientific).

The data were interpreted using the two-step Linderstrom-Lang model:

$$(\mathrm{N{-}^1H})_{\mathrm{closed}} \xleftrightarrow{k_{\mathrm{op}}/k_{\mathrm{cl}}} (\mathrm{N{-}^1H})_{\mathrm{open}} \xrightarrow{k_{\mathrm{int}}} \mathrm{N{-}^2H}$$

where k_{op} and k_{cl} are the rate constants for structural opening and closing, respectively, $(N – H)_{closed}$ corresponds to an exchange-protected state, and $(N – H)_{open}$ is the open form that exchanges with solvent at the intrinsic rate constant k_{int}. The measurable rate constant is $k_{ex} = k_{op} k_{int} / (k_{op} + k_{cl} + k_{int})$.

Under bimolecular exchange regime, corresponding to slow exchange ($k_{int} << k_{cl}$), k_{ex} reflects the equilibrium between the open and the closed states: $k_{ex} = k_{int}K_{op}$, where K_{op} is the equilibrium constant for structural opening (k_{op}/k_{cl}). Thus, under EX2 conditions, the free energy of structural opening is given by: $\Delta G_{HDX} = – RT \ln (k_{ex}/k_{int})$. The largest of the ΔG_{HDX} values are generally considered to represent the complete unfolding reaction, providing a reasonable estimate of the conformational stability of the observed protein.[54]

Fast exchange of amide protons with water was detected using a phase-modulated CLEAN chemical exchange spectroscopy (CLEANEX-PM)[55] pulse sequence on ^{15}N-labeled samples. Each 2D spectrum was recorded with spectral widths of 211.5 Hz with 2048 complex points in F2 and 2189.5 Hz over 128 complex points in F1, and with a mixing times of 75 ms.

^{15}N spin relaxation measurements

Protein backbone ^{15}N T_1, T_2, and steady-state {^{1}H}-^{15}N NOE experiments were recorded on [^{15}N]hL-FABP and its complexes with OLA and GCA. All relaxation experiments were performed in gradient-selected sensitivity-enhanced mode and in interleaved fashion, using a matrix of 2048 (^{1}H) × 128 (^{15}N) complex data-points for each relaxation delay (or for both NOE and NONOE) and spectral widths of 13 and 33 ppm in the ^{1}H and ^{15}N dimensions, respectively. Optimal water signal suppression was obtained with a flip-back pulse. Recycle delays of 3 s were used for T_1 and T_2, and of 6 s for NOE measurements. T_1 relaxation delays were 0.01, 0.18 (duplicate), 0.36, 0.54, 0.72, 0.90, 1.08, 1.26 (duplicate), 1.44 s. T_2 relaxation delays were 0.017, 0.034 (duplicate), 0.051, 0.068, 0.102, 0.137, 0.154, 0.171, 0.188 (duplicate), 0.205, 0.239 s. The delay in the Carr-Purcell-Meiboom-Gill pulse train was set to 0.45 ms. Peak volumes were measured employing the software CARA.[56] Relaxation times T_1 and T_2 were determined by fitting peak volumes to a single exponential decay using the computer program RELAXFIT.[57] The steady state {^{1}H}-^{15}N NOE parameters were computed from the ratio of peak volumes in NOE and NONOE spectra.

Residue-specific T_2/T_1 ratios were also predicted with the program HYDRONMR[36] based on the rotational diffusion tensor computed from the available atomic coordinates of hL-FABP and hL-FABP:OLA, assuming a rigid structure.

Relaxation dispersion experiments

Carr-Purcell Meiboom-Gill relaxation dispersion experiments were performed at a single static magnetic field strength of 600.13 MHz on 0.5 mM [^{15}N]hL-FABP in its unbound form and in complex with either GCA or OLA. A constant-time relaxation-compensated pulse program was used, setting the constant time period (T_{CPMG}) to 100 ms, in combination with the following CPMG frequencies (ν_{CPMG}): 40, 60, 80, 120, 160, 220, 360, 520, 700 and 840 Hz. Two-dimensional data sets were acquired in an interleaved manner, with 3 s inter-scan delay and 256 increments in the nitrogen dimension.

The observed transverse relaxation rate, R_2^{obs}, for each frequency point was obtained from the signal intensity measured at the end of the T_{CPMG} period according to:

$$R_2^{Obs} = -\frac{\ln\left(\frac{I_{\upsilon CPMG}}{I_0}\right)}{T_{CPMG}}$$

where I_0 is the signal intensity measured in a reference spectrum lacking the CPMG period and $I_{\nu CPMG}$ is the residual intensity at the end of the CPMG pulse sequence for a specific spin-lock frequency.

Relaxation dispersion curves were fitted assuming a simple two-state exchange process using the program NESSY.[58] A fast-limit (k_{ex} >> $\delta\omega$) and a slow-limit (k_{ex} << $\delta\omega$) exchange model between the sites were considered. In the fast-limit model the experimental data were fitted to:

$$R_2^{Obs} = R_2^0 + \frac{\Phi}{k_{ex}}\left[1 - \frac{4\upsilon_{CPMG}}{k_{ex}}\tanh\left(\frac{k_{ex}}{4\upsilon_{CPMG}}\right)\right]$$

where R_2^0 is the transverse relaxation rate constant in the absence of exchange, $\Phi = p_A p_B \delta\omega^2$, p_A and p_B are the fractional populations of the two states, k_{ex} is the chemical/conformational exchange constant and $\delta\omega$ the chemical shift difference between the two states.

In the slow-exchange model the relaxation dispersion curves were fitted to:

$$R_2^{Obs} = R_2^0 + \frac{k_{ex}}{2} - \upsilon_{CPMG}\cosh^{-1}\left[D_+\cosh(\eta_+) - D_-\cos(\eta_-)\right]$$

where:

$$D_\pm = \frac{1}{2}\left[\pm 1 + \frac{\Psi + 2\delta\omega^2}{\left(\Psi^2 + \xi^2\right)^{1/2}}\right]$$

$$\eta_\pm = \frac{\left[\pm\Psi + (\Psi^2 + \xi^2)^{1/2}\right]^{1/2}}{2\sqrt{2}\upsilon_{CPMG}}$$

$$\Psi = k_{ex}^2 - \delta\omega^2$$

$$\xi = -2\delta\omega\left(p_A k_{ex} - p_B k_{ex}\right)$$

Exchange parameters were then optimized using the Levemberg-Marquardt algorithm to minimize a target function and model selection was performed using Akaike information criteria with second order correction for small sample size. Uncertainties were estimated using 500 Monte Carlo simulations.

Data-driven docking

The structure calculations on the hL-FABP:GCA complex were performed using HADDOCK 2.1[59] in combination with CNS.[60] The twenty NMR conformers of hL-FABP (PDB: 2L68) were used as starting structures for the calculation. Parameters for the ligands were obtained from the PRODRG server.[61] The protein was kept fully flexible during docking while the ligand was kept rigid. During rigid body docking, 2000 structures were calculated. A total of 200 complex structures were selected after rigid body docking and subjected to optimization by fully flexible simulated annealing, followed by refinement in explicit water. Electrostatic and Van der Waals terms were calculated with a 8.5 Å distance cutoff using the OPLS non-bonded parameters from the parallhdg5.3.pro parameter file.[62] The resulting solutions were clustered using the algorithm of Daura *et al.*[63] with a 1 Å cut-off. The structures were divided in 10 clusters and the 4 best structures were selected for each cluster. The most representative structure of the complex was defined according to the lowest HADDOCK scores.

Acknowledgements

This work was funded by the Ministero dell'Istruzione, dell'Università e della Ricerca (FIRB 2008, Futuro in Ricerca, grant n. RBFR08R7OU, and PRIN 2009, grant n. 2009235JB7). FF acknowledges financial support by the Cooperint 2011 Internationalization program of the University of Verona.

Keywords: NMR spectroscopy · human liver fatty acid binding protein · bile salt · intracellular lipid transport · dynamics

[1] J. F. C. Glatz, J. J. F. P. Luiken, M. van Bilsen, G. J. van der Vusse, *Mol. Cell. Biochem.* **2002**, *239*, 3–7.
[2] J. F. Glatz, G. J. van der Vusse, *Prog. Lipid Res.* **1996**, *35*, 243–282.
[3] M. Furuhashi, G. S. Hotamisligil, *Nat. Rev. Drug Discov.* **2008**, *7*, 489–503.
[4] D. A. Bernlohr, M. A. Simpson, A. V. Hertzel, L. J. Banaszak, *Annu. Rev. Nutr.* **1997**, *17*, 277–303.
[5] C. Hohoff, F. Spener, *Lipid - Fett* **1998**, *100*, 252–263.
[6] A. W. Zimmerman, J. H. Veerkamp, *Cell. Mol. Life Sci.* **2002**, *59*, 1096–1116.
[7] M. E. Newcomer, *FASEB J.* **1995**, *9*, 229–239.
[8] A. Chmurzyńska, *J. Appl. Genet.* **2006**, *47*, 39–48.
[9] J. Thompson, N. Winter, D. Terwey, J. Bratt, L. Banaszak, *J. Biol. Chem.* **1997**, *272*, 7140–7150.
[10] Y. Xu, D. Long, D. Yang, *J. Am. Chem. Soc* **2007**, *129*, 7722–7723.
[11] A. Sharma, A. Sharma, *J. Biol. Chem.* **2011**, *286*, 31924–31928.
[12] J. Cai, C. Lücke, Z. Chen, Y. Qiao, E. Klimtchuk, J. A. Hamilton, *Biophys. J.* **2012**, *102*, 2585–2594.
[13] A. J. Levi, Z. Gatmaitan, I. M. Arias, *J. Clin. Invest.* **1969**, *48*, 2156–2167.
[14] J. Storch, *Mol. Cell. Biochem.* **1993**, *123*, 45–53.
[15] S. Mishkin, R. Turcotte, *Biochem. Biophys. Res. Commun.* **1974**, *57*, 918–926.
[16] B. P. Atshaves, G. G. Martin, H. A. Hostetler, A. L. McIntosh, A. B. Kier, F. Schroeder, *J. Nutr. Biochem.* **2010**, *21*, 1015–1032.
[17] J. Thompson, J. Ory, A. Reese-Wagoner, L. Banaszak, *Mol. Cell. Biochem.* **1999**, *192*, 9–16.
[18] S. Chuang, T. Velkov, J. Horne, C. J. H. Porter, M. J. Scanlon, *J. Med. Chem.* **2008**, *51*, 3755–3764.
[19] M. D'Onofrio, E. Gianolio, A. Ceccon, F. Arena, S. Zanzoni, D. Fushman, S. Aime, H. Molinari, M. Assfalg, *Chem. Eur. J.* **2012**, *18*, 9919–9928.
[20] L. Vergani, M. Fanin, A. Martinuzzi, A. Galassi, A. Appi, R. Carrozzo, M. Rosa, C. Angelini, *Mol. Cell. Biochem.* **1990**, *98*, 225–230.
[21] G. G. Martin, B. P. Atshaves, A. L. McIntosh, J. T. Mackie, A. B. Kier, F. Schroeder, *Biochem. J.* **2005**, *391*, 549–560.
[22] A. Dietrich, W. Dieminger, S. MacNelly, W. Gerok, G. Kurz, *J. Lipid Res.* **1995**, *36*, 1729–1744.
[23] M. Guariento, D. Raimondo, M. Assfalg, S. Zanzoni, P. Pesente, L. Ragona, A. Tramontano, H. Molinari, *Proteins* **2008**, *70*, 462–472.
[24] A. E. Thumser, D. C. Wilton, *Biochem. J.* **1996**, *320 (Pt 3)*, 729–733.
[25] G. P. Tochtrop, K. Richter, C. Tang, J. J. Toner, D. F. Covey, D. P. Cistola, *Proc. Natl. Acad. Sci. U.S.A* **2002**, *99*, 1847–1852.
[26] G. P. Tochtrop, G. T. DeKoster, D. F. Covey, D. P. Cistola, *J. Am. Chem. Soc.* **2004**, *126*, 11024–11029.
[27] O. Toke, J. D. Monsey, G. T. DeKoster, G. P. Tochtrop, C. Tang, D. P. Cistola, *Biochemistry* **2006**, *45*, 727–737.
[28] M. Pedò, M. D'Onofrio, P. Ferranti, H. Molinari, M. Assfalg, *Proteins* **2009**, *77*, 718–731.
[29] C. Cogliati, S. Tomaselli, M. Assfalg, M. Pedò, P. Ferranti, L. Zetta, H. Molinari, L. Ragona, *FEBS J.* **2009**, *276*, 6011–6023.
[30] S. Zanzoni, M. Assfalg, A. Giorgetti, M. D'Onofrio, H. Molinari, *J. Biol. Chem.* **2011**, *286*, 39307–39317.
[31] M. Guariento, D. Raimondo, M. Assfalg, S. Zanzoni, P. Pesente, L. Ragona, A. Tramontano, H. Molinari, *Proteins* **2008**, *70*, 462–472.
[32] J. Cai, C. Lücke, Z. Chen, Y. Qiao, E. Klimtchuk, J. A. Hamilton, *Biophys. J.* **2012**, *102*, 2585–2594.
[33] L. Fielding, *Curr Top Med Chem* **2003**, *3*, 39–53.
[34] Y. Shen, F. Delaglio, G. Cornilescu, A. Bax, *J. Biomol. NMR* **2009**, *44*, 213–223.
[35] V. A. Jarymowycz, M. J. Stone, *Chem. Rev.* **2006**, *106*, 1624–1671.
[36] J. García de la Torre, M. L. Huertas, B. Carrasco, *J. Magn. Reson.* **2000**, *147*, 138–146.
[37] A. G. Palmer 3rd, C. D. Kroenke, J. P. Loria, *Meth. Enzymol.* **2001**, *339*, 204–238.
[38] M. Pedò, M. D'Onofrio, P. Ferranti, H. Molinari, M. Assfalg, *Proteins* **2009**, *77*, 718–731.
[39] G. P. Tochtrop, K. Richter, C. Tang, J. J. Toner, D. F. Covey, D. P. Cistola, *Proc. Natl. Acad. Sci. U.S.A.* **2002**, *99*, 1847–1852.
[40] G. Horváth, P. Király, G. Tárkányi, O. Toke, *Biochemistry* **2012**, *51*, 1848–1861.
[41] S. Tomaselli, M. Assfalg, K. Pagano, C. Cogliati, S. Zanzoni, H. Molinari, L. Ragona, *Chemistry - A European Journal* **2012**, *18*, 2857–2866.
[42] Y. He, R. Estephan, X. Yang, A. Vela, H. Wang, C. Bernard, R. E. Stark, *Biochemistry* **2011**, *50*, 1283–1295.
[43] T. Mittag, L. Franzoni, D. Cavazzini, B. Schaffhausen, G. L. Rossi, U. L. Günther, *J. Am. Chem. Soc.* **2006**, *128*, 9844–9848.
[44] C. Cogliati, L. Ragona, M. D'Onofrio, U. Günther, S. Whittaker, C. Ludwig, S. Tomaselli, M. Assfalg, H. Molinari, *Chem. Eur. J.* **2010**, *16*, 11300–11310.
[45] M. E. Hodsdon, D. P. Cistola, *Biochemistry* **1997**, *36*, 1450–1460.
[46] C. Lücke, D. Fushman, C. Ludwig, J. A. Hamilton, J. C. Sacchettini, H. Rüterjans, *Mol. Cell. Biochem.* **1999**, *192*, 109–121.
[47] L. H. Gutiérrez-González, C. Ludwig, C. Hohoff, M. Rademacher, T. Hanhoff, H. Rüterjans, F. Spener, C. Lücke, *Biochem. J.* **2002**, *364*, 725–737.
[48] X. Zhang, X. Sui, D. Yang, *J. Am. Chem. Soc.* **2006**, *128*, 5073–5081.
[49] D. Long, D. Yang, *Biophys. J.* **2010**, *98*, 3054–3061.
[50] J. Lu, D. P. Cistola, E. Li, *J. Mol. Biol.* **2003**, *330*, 799–812.
[51] M. D'Onofrio, E. Gianolio, A. Ceccon, F. Arena, S. Zanzoni, D. Fushman, S. Aime, H. Molinari, M. Assfalg, *Chem. Eur. J.* **2012**, *18*, 9919–9928.
[52] J. F. Glatz, J. H. Veerkamp, *Anal. Biochem* **1983**, *132*, 89–95.
[53] P. Schanda, E. Kupce, B. Brutscher, *J. Biomol. NMR* **2005**, *33*, 199–211.
[54] Y. Bai, J. S. Milne, L. Mayne, S. W. Englander, *Proteins* **1993**, *17*, 75–86.
[55] T.-L. Hwang, S. Mori, A. J. Shaka, P. C. M. van Zijl, *J. Am. Chem. Soc.* **1997**, *119*, 6203–6204.
[56] R. L. J. Keller, *The Computer Aided Resonance Assignment Tutorial*, CANTINA, Goldau, CH, **2004**.
[57] D. Fushman, S. Cahill, D. Cowburn, *J. Mol. Biol.* **1997**, *266*, 173–194.
[58] M. Bieri, P. R. Gooley, *BMC Bioinformatics* **2011**, *12*, 421.
[59] C. Dominguez, R. Boelens, A. M. J. J. Bonvin, *J. Am. Chem. Soc.* **2003**, *125*, 1731–1737.
[60] A. T. Brünger, P. D. Adams, G. M. Clore, W. L. DeLano, P. Gros, R. W. Grosse-Kunstleve, J. S. Jiang, J. Kuszewski, M. Nilges, N. S. Pannu, et al., *Acta Crystallogr. D Biol. Crystallogr.* **1998**, *54*, 905–921.
[61] A. W. Schüttelkopf, D. M. F. van Aalten, *Acta Crystallogr. D Biol. Crystallogr* **2004**, *60*, 1355–1363.
[62] J. P. Linge, M. Nilges, *J. Biomol. NMR* **1999**, *13*, 51–59.
[63] X. Daura, K. Gademann, B. Jaun, D. Seebach, W. F. van Gunsteren, M. Alan E., *Angew. Chem. Int. Ed.* **1999**, *38*, 236–240.

Received: ((will be filled in by the editorial staff))

Entry for the Table of Contents (Please choose one layout)

Layout 1:

FULL PAPERS

Human liver FABP, an abundant cytosolic lipid carrier, displays ability to bind a variety of amphipathic molecules. NMR studies showed specific binding for glycocholate and provided structural and dynamic determinants of promiscuous binding capability.

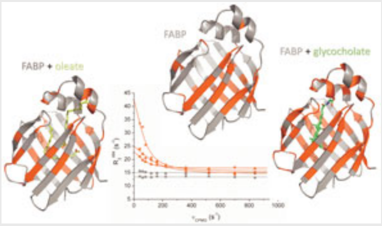

Filippo Favretto, Michael Assfalg, Mariana Gallo, Daniel Oscar Cicero, Mariapina D'Onofrio, and Henriette Molinari**

Page No. – Page No.

Ligand binding promiscuity of human liver fatty acid binding protein: structural and dynamic insights from an interaction study with glycocholate and oleate

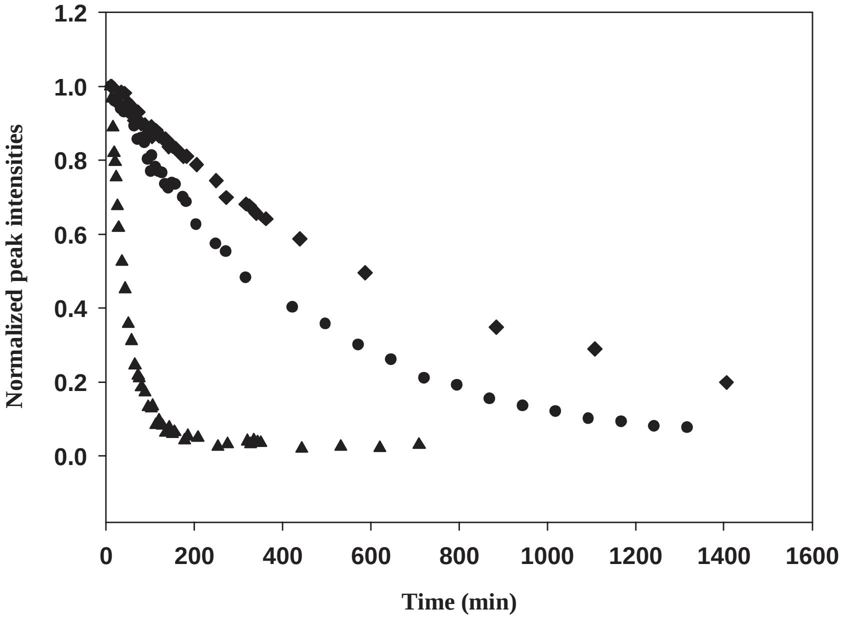

Figure S1: HDX exchange kinetic data of residue K90 in the apo hL-FABP ▲, in complex with GCA ♦, and with OLA ●. The data were obtained from the analysis of cross-peak intensities in ^{1}H,^{15}N-SOFAST-HMQC NMR experiments performed at 600.13 MHz on a 0.5 mM sample of [^{15}N]hL-FABP, p^{2}H 7.4.

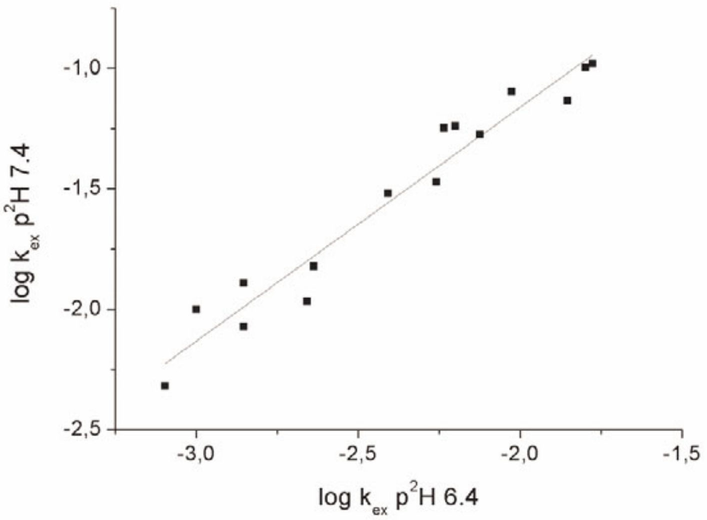

Figure S2: Plot of pH dependence of exchange. The value of log k_{ex} at p^{2}H 7.4 is plotted against the log kex at p^{2}H 6.41 for the same residue. The data relative to 15 residues could be compared. The experimental points were fitted with a linear regression: a slope of 0.97 ± 0.06 and an intercept of 0.8 ± 0.1 with R_2= 0.95 were obtained.

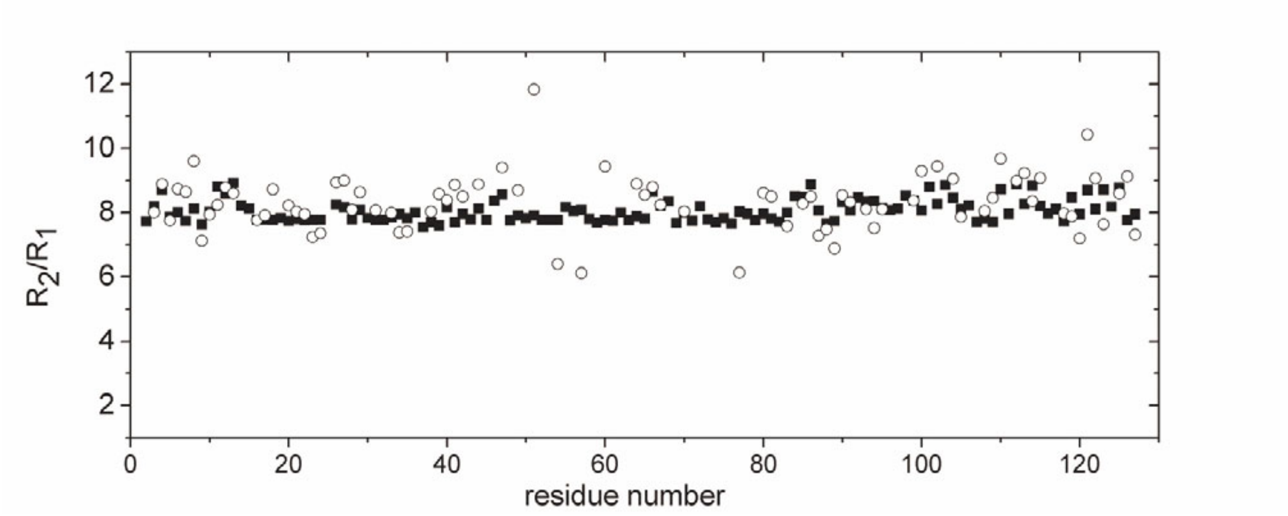

Figure S3. Plot of residue-specific R_2/R_1 for unbound hL-FABP. Data reported as black squares refer to predicted values calculated using HydroNMR based on the structure of hL-FABP (PDB: 2L67). Data reported as empty circles are experimental values.

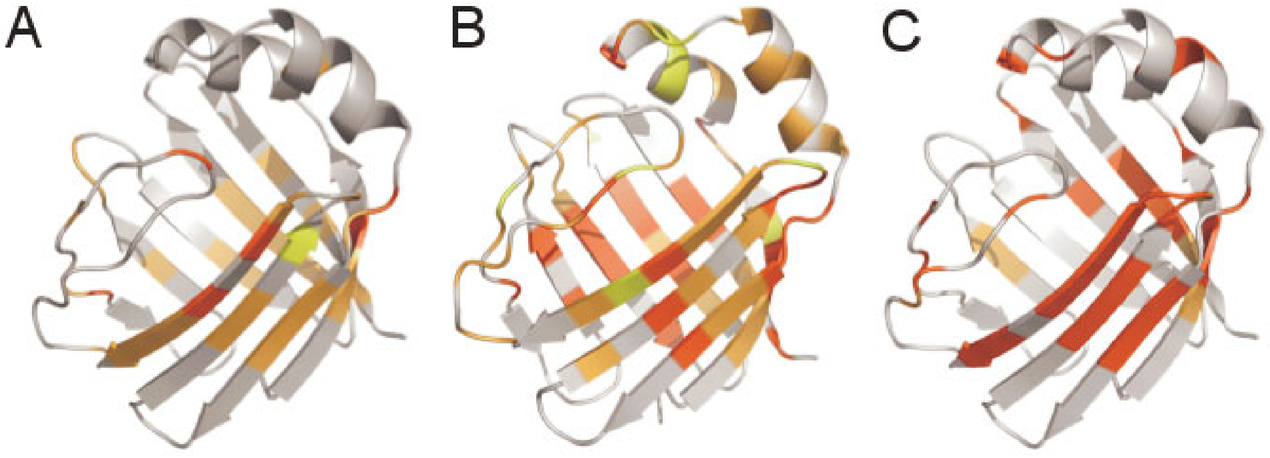

Figure S4: Experimental k_{ex}, derived from CPMG RD measurements, mapped onto the protein structure for A) apo hL-FABP, B) singly ligated GCA complex, C) doubly ligated OLA complex

Table S1. Summary of k_{ex}, and protection factors (P) derived from hydrogen exchange SOFAST NMR experiments at p^2H 7.4($p^2H = pH_{read} + 0.4$) for the hL-FABP in its apo form and in complex with GCA or OLA.

	APO		OLA		GCA	
Residue number and type	k_{ex} (min^{-1})[a]	P x 10^3	k_{ex} (min^{-1})	P x 10^3	k_{ex} (min^{-1})	P x 10^3
5 G	7.35±0.44E-02	20.58	1.0±0.02E-02	379.84	5.1±0.16E-02	29.65
7 Y	1.89±0.03E-02	15.36	SLOW[b]		7.0±0.21E-04	414.70
8 Q	3.09±0.05E-02	17.10	ND		1.88±0.06E-02	28.10
10 Q	1.046±0.047E-01	2.78	6.1±0.1E-03	119.53	1.18±0.083E-01	2.47
11 S	FAST[c]		1.4±0.073E-01	27.33	FAST	
18 F	4.9±0.08E-03	48.62	7.0±0.44E-04	854.75	1.7±0.027E-03	140.13
19 M	ND		SLOW		6.0±0.28E-04	774.21
20 K	ND		2.6±0.056E-03	465.40	3.8±0.074E-03	126.78
21 A	1.0±0.009E-02	54.05	3.0±0.05E-03	452.56	2.7±0.032E-03	200.20
22 I	3.00±0.006E-02	2.55	9.7±0.86E-05	1977.09	6.0±0.11E-04	127.26
24 L	5.66±0.07E-02	2.84	9.3±0.19E-03	43.46	1.98±0.03E-02	8.13
29 I	FAST		3.6±0.07E-02	3.28	FAST	
33 K	FAST		5.2±0.5E-03	267.17	FAST	
41 I	ND		ND		SLOW	
42 V	1.1±0.1E-03	43.60	ND		SLOW	
46 K	FAST		ND		FAST	
47 H	ND		2.4±0.03E-02	89.72	ND	
48 F	ND		ND		SLOW	
49 K	2.3±0.09E-03	188.03	SLOW		SLOW	
50 F	2.7±0.1E-03	62.92	ND		SLOW	
51 T	1.054±0.03E-01	3.86	4.0±0.35E-04	2556.30	2.37±0.03E-02	17.18
52 I	ND		ND		6.0±0.1E-03	20.17
53 T	FAST		ND		FAST	
56 S	ND		ND		FAST	
59 I	ND				5.2±0.064E-03	10.64
61 N	FAST		2.9±0.076E-03	1739.40	FAST	
63 F	FAST		SLOW		ND	
64 T	FAST		ND		FAST	
65 V	4.8±0.1E-03		ND		7.0±0.17E-04	184.42
66 G	1.01±0.032E-01	5.44	6.5±0.65E-02	21.24	3.51±0.05E-02	15.66
67 E	3.03±0.03E-02	6.27	1.6±0.02E-02	29.58	1.1±0.009E-02	17.27
69 C	ND		2.6±0.06E-02	117.24	1.18±0.02E-02	103.30
71 L	ND		ND		4.0±0.33E-04	193.95
72 E	ND		FAST		FAST	
73 T	ND		FAST		FAST	
74 M	ND		ND		FAST	
75 T	FAST		ND		FAST	
79 V	ND		3.7±0.14E-02	7.29	3.7±0.072E-03	29.02
80 K	FAST		ND		FAST	
81 T	2.87±0.05E-02	16.17	ND	13096.36		
83 V	1.28±0.02E-02	4.61	1.7±0.048E-03	87.18	1.2±0.02E-03	49.17
85 L	1.24±0.065E-01	1.39	1.2±0.068E-01	3.61	8.28±0.2E-02	2.08
86 E	ND		ND		FAST	
90 K	2.7±0.03E-02	28.94	2.3±0.04E-03	853.24	1.3±0.016E-03	601.02
91 L	1.51±0.02E-02	9.50	SLOW		SLOW	
92 V	1.11±0.02E-02	4.52	ND		ND	
93 T	1.63±0.03E-02	15.65	ND		7.0±0.12E-04	364.32
95 F	1.9±0.07E-03	125.38	FAST		FAST	
99 K	FAST		3.7±0.09E-02	14.95	5.46±0.15E-02	4.03
100 S	ND		ND		7.26±0.27E-02	17.45
101 V	1.12±0.02E-02	14.50	SLOW		3.0±0.1E-04	541.16

102	T	ND		ND		1.0±0.05E-04	2550.21
103	E			SLOW		2.0±0.2E-04	1017.91
104	L	3.37±0.06E-02	2.30	2.5±0.04E-02	7.76	ND	
108	I	ND		8.6±0.08E-03	14.76	ND	
109	I	6.2±0.2E-03	7.25	SLOW		SLOW	
110	T	8.5±0.2E-03	24.39	SLOW		1.7±0.042E-03	121.93
111	N	FAST		ND		1.16±0.02E-02	173.13
112	T	FAST		2.0±0.12E-04	9236.57		
113	M	ND		SLOW		FAST	
114	T	8.00±0.21E-02	5.67	ND		4.4±0.1E-02	10.31
115	L	5.77±0.12E-02	2.99	3.4±0.08E-02	12.74	2.81±0.08E-02	6.14
120	F	2.8±0.08E-03	61.63	SLOW		SLOW	
122	R	1.08±0.02E-02	59.72	ND		ND	
123	I	1.08±0.02E-02	11.73	ND		FAST	
124	S	ND		ND		molto lento	
125	K	FAST		1.3±0.75E-05	144014.24	3.9±0.056E-03	191.13
126	R	5.3±0.5E-02	12.17	5.4±0.33E-02	30.00	2.02±0.03E-02	31.93

[a] Reported errors refer to the errors in the least squares fitting.
[b] Residues defined as slow are still present in the last spectrum
[c] Residues defined as fast are not present already in the first spectrum

Table S2. Local fits of ^{15}N CPMG Dispersion for hLFABP apo

Residue	**k_{ex}(s^{-1})**	**Δω(ppm)**	**p_B**	**R_{ex} (s^{-1})**
7	382.9±78.8	0.32±0.25	0.3±0.09	7.4±0.9
8	444.5 ±52.9	0.51±0.18	0.3±0.10	14.9±0.8
9	761.2±111.7	0.41±0.4	0.3±0.12	6.6±0.3
14	502.3±39.5			6.2±0.3
29	616.3±54.3			5.9±0.3
36	1445.8±251.7			5.5±0.2
37	505.2±62.6	0.46±0.22	0.3±0.11	11.6±0.6
39	315.3±21.1			15.9±1.1
40	421.9±58.2	0.48±0.19	0.3±0.10	14.1±0.
41	376.1±67.0	0.41±0.22	0.3±0.10	11.7±1.1
50	377.5±58.5	3.27±0.04	0.05±0.001	17.6±0.3
51	103.4±9.3	1.40±0.02	0.3±0.02	21.0±0.6
53	27.9±56.7	2.10±0.12		4.7±0.7
55	394.3±78.6	0.35±0.26		8.6±1.0
57	326.6±35.0			9.5±1.0
58	777.5±51.6			7.3±0.3
60	933.7±41.2			10.3±0.2
61	23.7±20.8	1.03±0.10	0.3±0.01	5.0±0.8
62	664.1±24.2	0.88±0.08	0.3±0.05	28.5±0.3
63	64.2±10.5	1.47±0.02	0.3±0.03	13.3±0.6
65	493.0±82.1	0.37±0.27	0.3±0.11	8.0±0.6
75	908.1±150.2	0.43±0.50	0.3±0.13	5.9±0.3
79	500.0±37.6			6.8±0.3
82	553.4±25.7			12.2±0.4
83	2224.4±359.1	0.52±0.27	0.3±0.04	3.7±0.2
92	481.7±41.4	0.56±0.14	0.3±0.09	16.7±0.6
95	187.2±42.3			15.1±2.6
96	359.9±34.3			9.3±0.8
102	468.0±80.0	0.37±0.27	0.3±0.11	8.3±0.7
103	539.2±31.2			9.7±0.4
109	364.0±61.9	0.42±0.20	0.3±0.09	12.3±1.2
110	645.7±48.3			7.3±0.3
111	608.0±30.2			11.4±0.3
112	591.4±29.0			11.0±0.3
121	629.3±38.9			9.3±0.3
123	323.5±30.1			11.3±0.3
125	489.0±92.0	0.32±0.28	0.3±0.1	6.1±0.6

Table S3. Local fits of ^{15}N CPMG Dispersion for hLFABP-OLA

Residue	**k_{ex}(s^{-1})**	**Δω(ppm)**	**p_B**	**R_{ex} (s^{-1})**
7	625.8±57.6			6.0±0.3
8	1101.9±52.3			9.6±0.2
9	1502.0±212.5	0.60±0.66	0.3±0.13	7.3±0.2
12	910.6±57.5			7.4±0.2
14	633.6±55.8			6.3±0.3
22	2356.2±254.3	0.91±0.84	0.5±0.29	12.5±0.3
24	804.1±34.5			11.6±0.2
29	1164.1±45.0			11.4±0.2
30	729.4±74.3			5.0±0.3
36	1035.6±42.7			10.8±0.2
38	973.9±28.0			15.3±0.2
39	1147.9±56.4			9.6±0.2
40	841.1±46.6			8.8±0.2
41	833.8±43.4			8.8±0.2
50	1158.9±46.0			12.3±0.2
51	953.0±87.9	0.60±0.33	0.3±0.11	11.1±0.3
52	1400.9±76.2			8.4±0.2
54	1355.2±118.6			5.9±0.2
55	603.8±62.2			5.2±0.3
56	534.4±55.4			5.1±0.4
57	1036.5±40.7	0.99±0.14	0.3±0.07	25.5±0.2
58	3000.0±230.8	1.60±0.85	0.16±0.11	16.5±0.4
59	1008.3±126.3	0.53±0.45	0.3±0.13	8.3±0.3
60	1182.2±108.9	0.67±0.40	0.3±0.12	11.2±0.2
62	1253.0±50.8			12.0±
63	1274.5±79.7			8.0±0.2
69	500.0±36.2			5.9±0.3
70	1448.3±147.3			4.9±0.2
73	1690.4±137.3			6.4±0.2
79	1235.6±77.7	0.89±0.29	0.3±0.09	18.1±0.2
81	1673.2±59.8			14.6±0.2
92	638.7±31.9			10.3±
93	660.8±51.6			6.9±0.3
99	819.7±257.0	3.66±0.30	0.01±0.02	5.7±0.3
112	1053.6±82.8			6.3±0.2
115	3000.0±176.3	1.66±0.70	0.18±0.10	19.0±0.3
121	1260.4±185.0	0.55±0.58	0.3±0.13	7.1±0.2
122	783.3±49.2			7.8±0.3
123	733.8±34.7			11.2±0.3
124	257.5±46.0	0.34±0.13	0.3±0.05	11.1±1.4

Table S4. Local fits of ^{15}N CPMG Dispersion for hLFABP-GCA

Residue	**k_{ex}(s^{-1})**	**Δω(ppm)**	**p_B**	**R_{ex} (s^{-1})**
6	366.8±45.1			6.9±0.8
7	601.2±37.6			9.2±0.4
8	880.3±28.9			15.3±0.2
9	855.0±91.9	0.53±0.34	0.30±0.12	9.7±0.3
10	94.0±60.0	1.18±0.12	0.16±0.07	12.3±1.9
12	435.9±24.7			12.5±0.6
13	364.9±22.1			15.1±0.8
14	819.6±20.2			19.8±0.3
16	271.0±15.8			22.3±1.5
19	49.5±22.1	1.37±0.05	0.30±0.05	10.3±0.9
20	60.0±8.2	1.98±0.03	0.30±0.03	12.5±0.5
22	912.8±66.3			6.7±0.2
23	677.3±56.3			6.3±0.3
24	75.6±5.3	3.35±0.03	0.30±0.02	15.8±0.4
26	637.2±26.4	0.78±0.08	0.30±0.05	24.2±0.3
28	288.3±53.4	0.32±0.15	0.30±0.05	9.3±1.3
29	400.0±32.6	0.70±0.10	0.24±0.07	22.5±0.8
30	460.8±45.1			6.9±0.5
32	633.0±32.7	0.72±0.11	0.30±0.07	21.1±0.3
34	524.6±34.9			7.7±0.3
36	709.8±74.7	0.52±0.28	0.30±0.11	10.8±0.4
37	1441.6±46.0			16.0±0.2
38	934.1±32.4			13.7±0.2
39	100.8±34.6	1.96±0.05	0.14±0.05	12.1±0.8
40	114.3±24.2	2.34±0.04	0.19±0.03	17.3±0.8
41	809.0±34.1			11.7±0.2
48	512.3±28.2			8.8±0.3
50	1216.6±24.6			23.8±0.2
51	117.9±66.2	2.52±0.08	0.11±0.06	11.6±0.9
53	503.4±16.9			13.3±0.3
54	708.9±63.9	0.57±0.24	0.30±0.11	12.7±0.3
55	706.8±20.1			18.3±0.3
56	36.2±14.5	2.54±0.05	0.30±0.04	7.6±0.4
57	607.2±37.1			9.2±0.3
58	642.0±36.8			9.5±0.3
59	109.3±5.6	3.27±0.02	0.30±0.01	22.8±0.4
61	19.2±38.9	1.38±0.09	0.30±0.05	4.0±0.6
62	1067.0±24.2			20.6±0.2
65	527.0±13.6			22.3±0.4
66	221.0±90.1	0.71±0.26	0.13±0.08	15.0±3.4
68	508.8±28.3			8.5±0.3
69	354.0±54.8	0.50±0.17	0.30±0.09	16.9±1.4

71	170.3±48.5	1.55±0.05	0.08±0.03	11.4±0.6
72	720.1±20.6			18.0±0.3
73	41.8±10.6	2.68±0.06	0.30±0.04	8.8±0.5
74	205.3±37.4	0.52±0.12	0.30±0.05	20.9±2.5
75	125.6±28.4	2.37±0.04	0.17±0.03	17.3±0.8
77	244.2±23.4			19.0±2.2
80	20.5±43.3	2.95±0.10	0.30±0.06	4.3±0.4
81	521.9±15.3			19.2±0.4
83	3365.8±766.2			4.9±0.7
91	267.9±48.6	0.44±0.16	0.30±0.07	16.0±1.9
93	361.7±26.2			12.1±0.8
95	723.4±71.3	1.85±0.13	0.05±0.01	18.0±0.3
98	730.7±38.1			9.4±0.3
99	560.7±58.8	0.53±0.20	0.30±0.10	13.6±0.5
100	892.1±59.7	0.71±0.22	0.30±0.09	15.8±0.3
101	2710.7±132.5			15.0±0.3
102	1586.7±126.6	0.85±0.46	0.30±0.12	13.2±0.2
104	672.3±59.0			5.9±0.3
109	69.4±50.4	3.27±0.08	0.18±0.06	10.1±0.9
110	720.1±20.1			18.0±0.3
111	244.5±79.6	1.41±0.11	0.05±0.02	9.0±0.6
112	730.4±28.4			13.4±0.3
113	720.5±56.1	0.61±0.21	0.30±0.10	14.1±0.3
115	380.9±41.9	1.46±0.06	0.07±0.01	15.8±0.4
121	1028.7±71.7	0.74±0.27	0.30±0.10	15.2±0.3
122	744.5±53.2			7.3±0.3
124	346.1±39.2			8.7±1.0
126	1297.4±331.2	1.98±0.85	0.02±0.12	5.5±0.3